Energy consumption in desalinating produced water from shale oil and gas extraction

Citation: Thiel, Gregory P., Emily W. Tow, Leonardo D. Banchik, Hyung Won Chung, and John H. Lienhard. "Energy Consumption in Desalinating Produced Water from Shale Oil and Gas Extraction." Desalination 366 (June 2015): 94–112.

As Published: http://dx.doi.org/10.1016/j.desal.2014.12.038

Publisher: Elsevier

Persistent URL: http://hdl.handle.net/1721.1/101978

Version: Author's final manuscript: final author's manuscript post peer review, without publisher's formatting or copy editing

Energy consumption in desalinating produced water from shale oil and gas extraction

Gregory P. Thiel[a], Emily W. Tow[a], Leonardo D. Banchik[a], Hyung Won Chung[a], John H. Lienhard V[a,*]

[a] *Rohsenow Kendall Heat Transfer Laboratory, Department of Mechanical Engineering, Massachusetts Institute of Technology, Cambridge, MA 02139-4307, USA*

Abstract

On-site treatment and reuse is an increasingly preferred option for produced water management in unconventional oil and gas extraction. This paper analyzes and compares the energetics of several desalination technologies at the high salinities and diverse compositions commonly encountered in produced water from shale formations to guide technology selection and to inform further system development. Produced water properties are modeled using Pitzer's equations, and emphasis is placed on how these properties drive differences in system thermodynamics at salinities significantly above the oceanic range. Models of mechanical vapor compression, multi-effect distillation, forward osmosis, humidification-dehumidification, membrane distillation, and a hypothetical high pressure reverse osmosis system show that for a fixed brine salinity, evaporative system energetics tend to be less sensitive to changes in feed salinity. Consequently, second law efficiencies of evaporative systems tend to be higher when treating typical produced waters to near-saturation than when treating seawater. In addition, if realized for high-salinity produced waters, reverse osmosis has the potential to achieve very high efficiencies. The results suggest a different energetic paradigm in comparing membrane and evaporative systems for high salinity wastewater treatment than has been commonly accepted for lower salinity water.

Keywords: energy efficiency; hydraulic fracturing; frack water; high salinity; produced water remediation

*Corresponding author
Email address: lienhard@mit.edu (John H. Lienhard V)

Nomenclature

Roman Symbols

a	Activity
b	Molality, mol/kg
c_p	Specific heat capacity, kJ/kg-K
e	Elementary charge, $1.602\ 176\ 565(35) \times 10^{-19}$ C
G; g; $\bar{g}$	Gibbs free energy, J; J/kg; J/mol
h	Specific enthalpy, kJ/kg
h_{fg}	Enthalpy of vaporization, kJ/kg
I	Ionic strength, mol/kg
k_b	Boltzmann constant, J/K
M	Molar mass, kg/mol
MR	Mass flow rate ratio
m	Mass, kg
$\dot{m}$	Mass flow rate, kg/s
$\dot{N}$	Molar flow rate, mol/s
N_0	Avogadro's number, mol^{-1}
$\dot{Q}$	Heat transfer rate, W
P	Pressure, Pa
PR	Pressure ratio
R	Gas constant, J/mol-K or J/kg-K
RR, $\overline{\text{RR}}$	Mass- and mole-based recovery ratio
T	Temperature, K
V	Volume, m^3/mol or m^3/kg
$\dot{W}$	Work transfer rate, W
w	Mass fraction

Greek Symbols

α	Pitzer parameter, $\text{kg}^{\frac{1}{2}}/\text{mol}^{\frac{1}{2}}$
β_w	Isothermal compressibility, Pa^{-1}
$\beta_{ij}^{(0)}, \beta_{ij}^{(1)}$	Pitzer parameter, kg/mol
γ	Ratio of specific heats
$\gamma_{\pm}$	Mean molal activity coefficient
δ	Boiling point elevation, K
ϵ_r	Relative permittivity
ϵ_0	Vacuum permittivity, F/m
η	Efficiency
$\dot{\Xi}$	Exergy flow rate
Π	Osmotic pressure, bar
ρ	Density, kg/m^3
ϕ	Osmotic coefficient
ω	Humidity ratio, $\text{kg}_\text{v}/\text{kg}_\text{da}$

Subscripts

0	Environment state
B	Bottom
b	Brine stream
C	Compressor
D	Dehumidifier
d	Draw stream
da	Dry air
dc	Concentrated draw stream

dd	Diluted draw stream
EC	Evaporator-Condenser
eff	Effective
f	Feed stream
H	High pressure, Humidifier
i	Inlet
ib	Intermediate brine
im	Intermediate value
ma	Moist air
o	Outlet
P	Pump
p	Product (fresh or treated) stream
pp	Pinch point
PX	Pressure exchanger
rec	Recovered
s	Salt
T	Top
t	Terminal
v	Vapor
w	Pure water

Superscripts

ex	Excess thermodynamic quantity
s	Saturated state
$\circ$	Standard state
$\star$	Optimum value

1. Introduction

A combination of reduced conventional reserves, policy changes, and advances in drilling technology has paved the way for a natural gas boom in North America. Much of this new resource is recovered using an unconventional technique known as hydraulic fracturing, in which small fissures are created in a narrow, tight shale layer, allowing associated hydrocarbons to flow more freely. This process both consumes and produces large amounts of water. The challenges associated with disposal and sourcing of this water are driving increased recycling and reuse, part of which is achieved by desalination.

Hydraulic fracturing works as follows. A vertical well is drilled to a depth of 1500–4500 m where it turns horizontally into a shale layer which may be as narrow as tens of meters in height. A steel and cement casing is installed along the entire length of the bore. Then, a shaped-charge device known as a perforating gun creates holes in the casing and the surrounding shale layer. Finally, the shale layer is fractured using a high pressure mixture of sand, water, and chemical additives pumped down the well. The resulting fissures release the hydrocarbons trapped in the shale.

Anywhere from 7,600–25,000 m^3 (2–6.5 million gallons) [1, 2] of water are used in the water-sand-chemical mixture [3] needed to perform a single fracture. Depending on the formation and well, between 30–70% of this mixture [2] returns to the surface within several weeks and has relatively low salinities; a smaller, more saline flow will return steadily over the life of the well along with the oil and/or gas. The former stream is known as flowback, and the latter as produced water. The U.S. generates an estimated 3.3 billion cubic meters per year of produced water from conventional and unconventional oil and gas sources [4]. Accounting for the portion attributable to unconventional gas is difficult, but with 60% of U.S. natural gas production attributed to unconventional resources [5] and an average water-to-gas ratio of 1.46 L/m^3 [4], we might roughly estimate unconventional produced water generation to be around 570 million cubic meters per year.

The low-salinity flowback is often reused with no or minimal treatment [6, 7]. In contrast, produced water may be hypersaline, with salinities as high as seven times seawater; this water generally must be treated or disposed of. Produced water disposal is usually by deep well injection; however, this process can be costly, particularly when wastewater must be trucked large distances to a disposal well [8]. Disposal of produced water is also surrounded by environmental concerns, with deep well injection linked to increased seismicity in several locations in the U.S. [9–13].

On-site desalination is a part of the produced water management solution that can address both environmental and economic challenges [14]. But in spite of a general trend towards reuse and work towards formalizing a water treatment selection process [15, 16], no overarching industry standard yet exists on what treatment processes are necessary or best-suited for particular waters, or on the extent to which wastewater must be treated before reuse. Furthermore, solutions for desalinating hypersaline produced water streams in particular are unstandardized, with no clear and dominant choice among emerging and established technologies.

In this work, we provide models for calculating the energy consumption of produced water desalination technologies at high salinity and variable water composition in order to: (1) provide a baseline method for energetic comparison of produced water desalination technologies; (2) aid in the development of thermoeconomic models that will better inform technology selection; and (3) provide a basis for further system research and development.

2. A Thermoeconomic Framework for Assessment of Produced Water Desalination Systems

In this section, we develop a simple thermoeconomic framework that informs the choice of thermodynamic figures of merit. We argue that when reuse is economically viable, recovery ratios should be maximized, and that energy consumption should be normalized per unit product water. We then discuss how composition affects energy consumption and the maximum recovery ratio attainable. Finally, we use these components to develop an approach to compare the energetics of desalination systems at produced water salinities.

2.1. Economic Rationale for Reuse

Where a regulatory framework does not compel a particular reuse or disposal process, economics will dictate the extent and type of reuse. The net water cost to a field operator is the sum of sourcing, reuse (if present), and disposal costs. In general, a reuse system splits a wastewater feed stream into a brine (or

solids) and purer product stream. Depending on the reuse strategy, the net cost of reuse may be reduced by the sale of valuable brine [17], blending, or partial desalination [18]. In spite of the feed stream's disposal cost and the potential value of the brine and product streams, it is the product stream alone that reduces the quantities of both the water sourced and disposed. Thus, either high disposal or high sourcing costs can motivate reuse. More precisely, the net cost of reuse *per unit product* must be less than the unit cost of sourcing and disposal for reuse to be economically justifiable. Consequently, the energy consumption, which is directly proportional to the net energetic cost, should also be normalized per unit of product.

In addition, because produced water desalination is a waste concentration process, recovery ratios (the ratio of product to feed stream mass flow rates, $\mathrm{RR} = \dot{m}_p/\dot{m}_f$) should generally be maximized. Thus, for any desalination component of a reuse strategy, we require models describing energy consumption per unit water produced and a method to determine the maximum recovery attainable, both of which depend on the produced water composition.

2.2. Modeling Produced Water Properties

Produced water composition and total salinity vary widely, not only from formation to formation, but even from well to well [1, 19, 20], making it impossible to standardize the composition. Nevertheless, the major components of the water show patterns. In the samples presented in [19, 20], sodium and chloride make up the largest mass fraction of dissolved material, and about 95–98% of the solutes on a molal scale are made up of calcium, sodium, and chloride ions. Other components are present in amounts less than 1%. Although these minor components will impact system design through, e.g., scaling considerations, they will not affect the separation energy significantly. We thus propose that, for the purposes of thermodynamic analyses, the thermophysical properties of the water are mostly characterized by considering mixtures of Ca-Na-Cl, in varying amounts. Because the addition of up to 10% calcium changes the properties only slightly (as shown below), we will only consider aqueous sodium chloride in the present work.

Thermophysical properties that affect the energy consumption of systems analyzed here include: density (ρ), specific heat capacity (c_p), boiling point elevation (δ), and osmotic pressure (Π), all of which vary significantly over broad ranges of salinity. For an arbitrary mixture, these properties are computed according to:

$$\rho = \frac{1000[\mathrm{kg/m^3}] + \sum_i b_i M_i}{1000[\mathrm{kg/m^3}]/\rho_w + \sum_i b_i \bar{V}_i^\circ + V^{\mathrm{ex}}} \tag{1}$$

$$c_p = \frac{\bar{c}_{p,w}^\circ}{M_w} + \sum_i b_i \bar{c}_{p,i}^\circ + c_p^{\mathrm{ex}} \tag{2}$$

$$\delta = \frac{RT^2\phi\sum_i b_i}{h_{fg}} \tag{3}$$

$$\Pi = RT\phi\rho_w \sum_i b_i \tag{4}$$

where b is molality, M is molar mass, R is the universal gas constant, ϕ is the osmotic coefficient, V is volume, and h_{fg} is the enthalpy of vaporization of pure water. The superscript $\circ$ denotes the standard state, which for aqueous species is the usual convention of ideal solution behavior as the molality of the solute approaches zero; the superscript 'ex' denotes an excess property. A bar over a property indicates it is written on a molar basis, and the sums should be performed over all i solutes.

To compute these properties, we require models for the excess volume, the excess heat capacity, and the osmotic coefficient that can be used for electrolytes at high ionic strengths. We use Pitzer's equations [21, 22] for this purpose, which are outlined in Appendix A.1 and have been validated for a wide array of single and mixed electrolytes over a range of concentrations from dilute to saturation [23, 24]. Pure water properties are from the International Association for the Properties of Water and Steam (IAPWS) [25] formulation.

The boiling point elevation and osmotic pressure of aqueous NaCl is shown in Fig. 1, with comparison to design-case samples from [20] for two major shale formations: the Permian Basin and the Marcellus. For the Permian sample, which is mostly NaCl, pure NaCl represents a good approximation to δ and Π; in the Marcellus, where Ca^{2+} concentrations are higher, an Na-Ca-Cl mixture is a better approximation. Although the boiling point elevation (BPE) may be small relative to stage to stage ΔT and terminal temperature

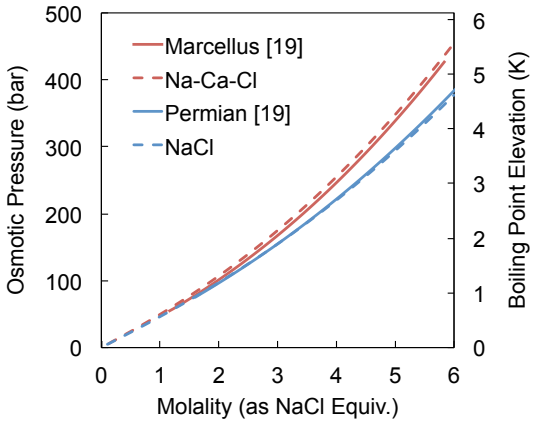

Figure 1: Thermophysical properties of produced water that affect energy consumption in desalination systems: boiling point elevation and osmotic pressure of typical samples from [20] are well-represented by considering pure NaCl. When Ca^{2+} concentrations are high, as for the Marcellus shale produced water, a mixture of Na-Ca-Cl in appropriate quantities is a better abstraction of a real sample.

differences in seawater desalination systems [26], the larger values of BPE at higher salinities will lead to a more significant energy penalty on imbalanced, low-pinch thermal systems such as multistage flash (MSF) or multi-effect distillation (MED). The osmotic pressure near saturation, which sets the top pressure in reverse osmosis systems, is more than six times higher than the osmotic pressure of the brine in typical seawater systems at 50% recovery.

With appropriate measures for scale control, the practical maximum recovery ratio is generally dictated by sodium chloride saturation, as it is normally the dissolved compound with the greatest concentration. If scaling or any salt crystallization does not occur, the achievable recovery ratio is related to the concentration of a salt in the feed and brine streams. Setting the concentration of NaCl in the brine stream to its saturated value yields the following expression for maximum recovery ratio:

$$\mathrm{RR}_{\max} = w_{w,f}\left(1 - \frac{b_{\mathrm{NaCl},f}}{b_{\mathrm{NaCl,sat}}}\right) = w_{w,f}\left(1 - \frac{\gamma_{\pm,\mathrm{NaCl,sat}} b_{\mathrm{NaCl},f}}{\sqrt{K_{sp}}}\right) \tag{5}$$

where $w_{w,f}$ is the mass fraction of water in the feed, $\gamma_{\pm,\mathrm{NaCl,sat}}$ is the mean molal activity coefficient of NaCl in the particular produced water mixture at saturation, and K_{sp} is the solubility product.

Because the value of $\gamma_{\pm,\mathrm{NaCl,sat}}$ will change depending on the exact produced water composition, the exact recovery ratio at which sodium chloride saturation occurs will depend on the exact composition. However, because most species other than Ca^{2+}, Na^+, and Cl^- are present in small amounts ($\lesssim 1\%$), their contribution to the NaCl activity coefficient is small. Thus, the solubility of NaCl in most produced waters is well-approximated by consideration of the Ca-Na-Cl system alone. We thus set the brine salinity in our analyses to a fixed value of 6.01 mol/kg solvent, or 26% by mass (corresponding to saturation for pure aqueous NaCl), except where noted.

2.3. Least Work of Separation

To evaluate the efficiency of these systems, the least work of separation is required. When the feed f, product p, and brine b streams are all at the same temperature and pressure, the least work of separation is given by the first and second laws of thermodynamics in terms of the Gibbs free energy:

$$\frac{\dot{W}_{\mathrm{least}}}{\dot{N}_{w,p}} = (\bar{g}_p - \bar{g}_b) - \frac{1}{\overline{\mathrm{RR}}}(\bar{g}_f - \bar{g}_b) \tag{6}$$

where $\dot{N}_{w,p}$ is the molar flow rate of pure water in the product stream and $\overline{\mathrm{RR}}$ is the molar-flow-rate-based recovery ratio. Mistry et al. [27–29] have analyzed the effect of composition on least work requirements in

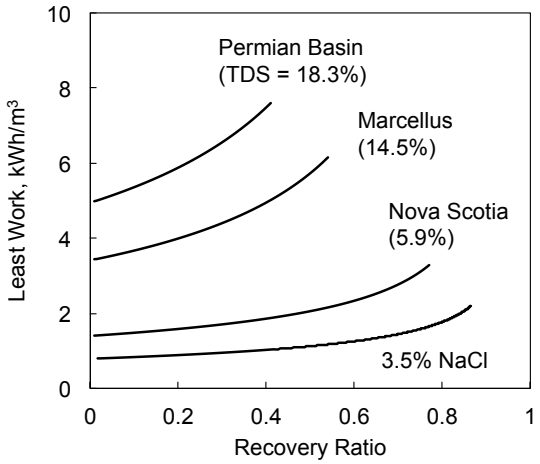

Figure 2: Least work of separation versus recovery ratio for three representative produced water samples [20] and a 3.5% (by mass) NaCl solution representing seawater: the least work for produced water can be nearly an order of magnitude higher than the 1 kWh/m^3 rule-of-thumb for seawater at 50% recovery.

detail, and they provide a general expression for least work of separation applicable to any ionic composition in the absence of chemical reactions:

$$\frac{\dot{W}_{\text{least}}}{\dot{N}_{w,p}RT} = \left(\ln\frac{a_{w,p}}{a_{w,b}} + \sum_i b_{i,p}M_w \ln\frac{a_{i,p}}{a_{i,b}}\right) - \frac{1}{\overline{\text{RR}}}\left(\ln\frac{a_{w,f}}{a_{w,b}} + \sum_i b_{i,f}M_w \ln\frac{a_{i,f}}{a_{i,b}}\right) \tag{7}$$

where a is the activity, the subscript w denotes the solvent (water), and the subscript i denotes a solute. For a pure product, the molality of salts in the product stream is zero, and the second term in the first set of parentheses vanishes. The mass-based recovery ratio is related to the mole-based quantity as $\text{RR} = \overline{\text{RR}} \times M_w/M_f$, where the average molar mass of the feed stream $M_f = 1/(w_{w,f}/M_w + \sum_i w_{i,f}/M_i)$.

A plot of Eq. (7) versus recovery ratio for three types of produced water is shown in Fig. 2. The produced water from the Maritimes Basin in Nova Scotia has higher salinity than seawater [19]; its line thus continues to lower recovery ratios, but requires more energy. Owing to its extremely high salinity, the water from the Permian Basin, in contrast, requires nearly five times as much work to treat at zero recovery. The rule-of-thumb value for the least work required to treat seawater at 50% recovery is 1 kWh/m^3, but we see that in the case of produced water, the least work may be nearly an order of magnitude higher.

2.4. Second Law Efficiency

For a desalination system, the second law efficiency is the ratio of the least work required to separate a feed stream into a brine and product stream to the actual exergy input to the system [28]:

$$\eta = \frac{\dot{W}_{\text{least}}}{\dot{W}_i + (1 - T_0/T_H)\dot{Q}_i} \tag{8}$$

where $\dot{W}_i$ and $\dot{Q}_i$ are the net work and heat inputs to the system, respectively, T_0 is the temperature of the environment, and T_H is the temperature from which the heat transfer Q_i to the system occurs.

In seawater desalination, fresh water is the single useful product, and a reversible system operating at zero recovery corresponds to the lowest energetic cost to obtain any number of units of fresh water from seawater. For seawater desalination systems, as described in detail in [30], the minimum least work, $\dot{W}_{\text{least}}^{\text{min}} = \lim_{\text{RR}\to 0}\left(\dot{W}_{\text{least}}\right)$, is therefore the appropriate efficiency datum. However, in produced water desalination, the concentration of the feed, the brine stream, and the reuse of the product stream all have

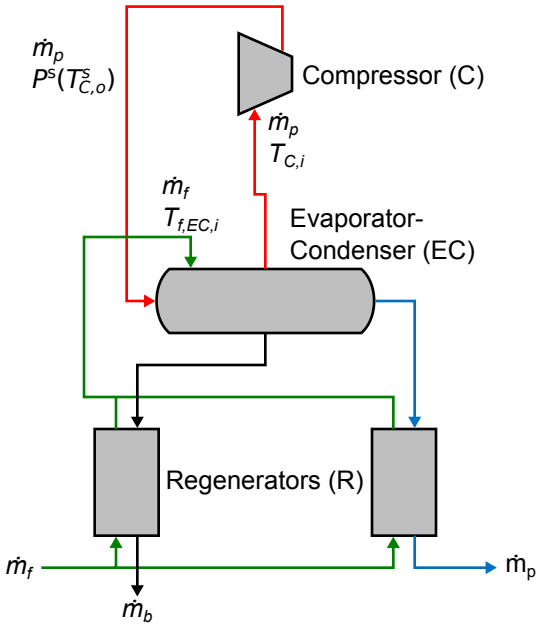

Figure 3: Schematic diagram of a typical MVC system: a saline feed is preheated in regenerators and sprayed over warm tubes in the evaporator condenser (EC), causing evaporation. This pure vapor is compressed and condenses inside tubes in the EC to produce pure water.

potential economic value. A zero recovery produced water desal system would not be useful because it does not reduce the waste volume or decrease the source water volume or create saturated (or near-saturated) brine. From the perspective of waste concentration, it is the brine flow relative to the feed that has value; from the perspective of reuse it is the product flow relative to the feed that has value. Consequently, the efficiency datum in produced water desalination is the least work at finite, non-zero recovery.

In the present definition, because the brine salinity is fixed and only pure product is considered, recovery ratio is unchanged when comparing systems at a particular feed salinity. Therefore, the numerator of efficiency is the same across systems compared at equal feed salinity, and the ratio of two system efficiencies will be independent of the chosen datum.

3. Systems Analyses

The framework developed in Sec. 2 is applied to simple models for several types of desalination systems to understand their behavior at produced water salinities. Because high recovery ratios are desirable and feed salinity is highly variable—spatially (i.e., well to well) and temporally [1]—we assess the dependence on feed salinity as follows. For each technology, the brine salinity is fixed at the value corresponding to maximum recovery ($w_{s,b} = 26\%$) except where noted, and the feed salinity is varied. Specific energy consumption and efficiency are then calculated over the feed salinity domain. Finally, system efficiencies are compared.

3.1. Mechanical Vapor Compression

Mechanical vapor compression (MVC) is one of the most established technologies considered here, and it is widely deployed to treat seawater and higher-salinity feeds at a variety of scales. A schematic diagram of a typical MVC system is shown in Fig. 3. A saline feed stream is preheated in a regenerator and sprayed over warm coils in the evaporator/condenser (EC), resulting in the evaporation of pure water. The vapor is compressed to a higher pressure and temperature and fed back into the EC where it desuperheats and condenses to provide the heat for the vaporization process. The resulting brine and product streams preheat the saline feed stream in regenerators.

The net energy consumption of MVC is the sum of the electrical work required to drive the compressor and circulation pumps. However, most of the energy consumption in MVC is the compressor. A simple model for computing the energy consumption follows.

The pressure ratio in the compressor can be written as the ratio of pure water saturation pressures corresponding to the temperatures required drive the evaporation process in the EC. From the Clausius-Clapeyron equation with the usual ideal gas approximation,[1] the pressure ratio is

$$\mathrm{PR} = \exp\left[-\frac{h_{fg}}{R_w}\left(\frac{1}{T^s_{C,o}} - \frac{1}{T^s_{C,i}}\right)\right] \tag{9}$$

where T^s is the pure water saturation temperature corresponding to the pressure at the compressor inlet (C,i) and compressor outlet (C,o) and $R_w = R/M_w$ is the gas constant of water. At the EC inlet, the feed is a saturated liquid at $T_{f,EC,i}$, which is above the normal saturation temperature by the boiling point elevation of the feed, δ_f. Thus, the compressor suction pressure is the vapor pressure of pure water at $T^s_{C,i}$:

$$T^s_{C,i} = T_{f,EC,i} - \delta_f \tag{10}$$

As the pure vapor evaporates from the feed stream at constant pressure in the EC, the feed stream temperature increases by an amount $\delta_b - \delta_f$ as it reaches the brine salinity. The pressure at the compressor outlet must be set high enough that the condensing (pure) stream in the EC remains above the evaporating stream by a terminal temperature difference (ΔT_t) when the evaporating stream is at its most concentrated (brine) state. Therefore,

$$T^s_{C,o} = T_{f,EC,i} + \delta_b - \delta_f + \Delta T_t \tag{11}$$

The vapor at the compressor inlet is superheated at pressure $P^s(T^s_{C,i})$ and temperature $T_{C,i}$. The compressor inlet temperature $T_{C,i}$ corresponds to a bulk enthalpy that is averaged across the evaporating vapor, but we take it simply as the average of the feed inlet and brine outlet temperatures in the EC:

$$T_{C,i} = T_{f,EC,i} + \frac{1}{2}(\delta_b - \delta_f) \tag{12}$$

because we cannot evaluate the fraction of vapor produced as a function of temperature without introducing a heat transfer model and system dimensions.

The compressor work can be expressed as the isentropic work of compression divided by a compressor efficiency:

$$\frac{\dot{W}}{\dot{m}_p} = \frac{c_{p,v}T_{c,i}}{\eta_c}\left[\mathrm{PR}^{\frac{\gamma-1}{\gamma}} - 1\right] \tag{13}$$

where PR is the pressure ratio in the compressor, η_c is the compressor efficiency, and $c_{p,v}$ is the specific heat of pure water vapor. Substituting Eqs. (9),(10), and (11) into Eq. (13), we find

$$\frac{\dot{W}}{\dot{m}_p} = \frac{c_{p,v}}{\eta_c}\left[T_{f,ec,i} + \frac{1}{2}(\delta_b - \delta_f)\right] \tag{14}$$

$$\times\left\{\exp\left[-\frac{h_{fg}}{c_{p,v}}\left(\frac{1}{T_{f,ec,i} + \delta_b - \delta_f + \Delta T_t} - \frac{1}{T_{f,ec,i} - \delta_f}\right)\right] - 1\right\} \tag{15}$$

Thus, the energy consumption of an MVC system is completely specified by an evaporator-condenser pressure, the terminal temperature difference in the EC, the feed and brine salinities, and a compressor efficiency.

From Eq. (15), we see that the primary effect of salinity change on energy consumption is an increase in the required pressure ratio in the compressor. This increase is driven by two compounding effects: a reduction in evaporating vapor pressure as salinity increases and a higher discharge pressure in order to maintain a finite temperature difference across the evaporator-condenser as the feed warms and becomes more saline. The latter essentially increases irreversibility associated with imbalance in the evaporator-condenser. The change in boiling point elevation within the evaporator, $\delta_b - \delta_f$, may approach ΔT_t in high recovery cases.

[1] Compared to the Saul and Wagner equation for vapor pressure [31], this set of approximations underpredicts the PR by $\lesssim 0.6\%$ over the temperature domain considered here.

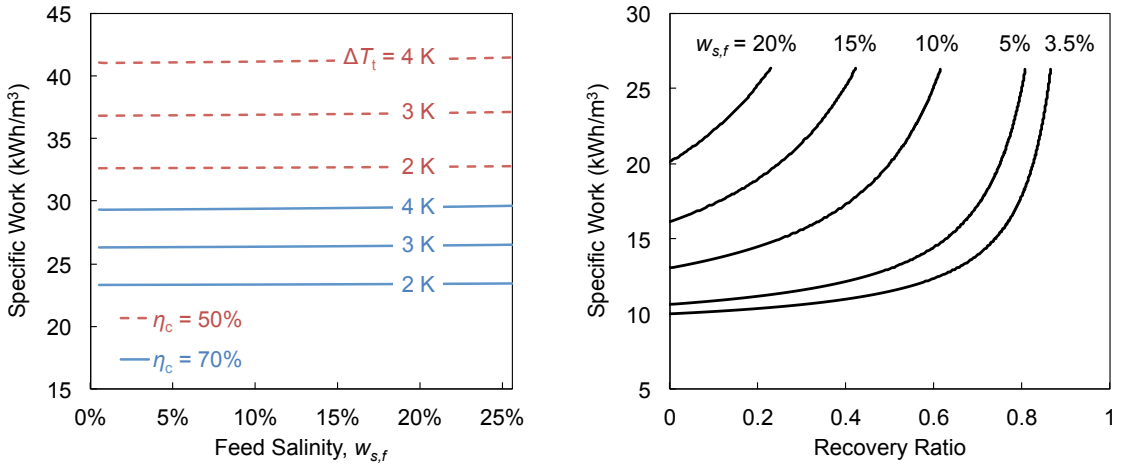

(a) $w_{s,b} = 26\%$ (b) $\Delta T_t = 3$ K

Figure 4: Specific energy consumption for MVC over the salinity domain: (a) At fixed brine salinity, the energy consumption of MVC is fairly insensitive to changes in feed salinity, because the brine salinity sets the compressor discharge pressure. (b) When brine salinity is not fixed, energy consumption rises with increasing feed salinity and recovery ratio.

For a typical compressor efficiency[2] of 70% and $T_{f,ec,i} = 60\,^{\circ}\mathrm{C}$, a plot of Eq. (15) in Fig. 4a shows only a small increase in energy consumption with feed salinity. At fixed brine salinity, the compressor discharge pressure is fixed, so the energy consumption of the system is more sensitive to ΔT_t over the range here. However, because the least work of separation is significantly more sensitive to salinity, we see that MVC is operating much closer to its reversible limit at higher feed salinities, as shown in Fig. 5. Thus, although MVC is generally considered to be low-efficiency [30] (relative to RO) in the seawater range, it operates at higher efficiency at higher salinities.

The rise in MVC efficiency with salinity results from the effects of salinity on BPE and temperature pinch. At low salinities, the BPE rise in the EC, representing the reversible work of separation, is small compared to the driving force for (irreversible) heat transfer, which is related to ΔT_t. When the irreversible work is larger than the reversible work, efficiency is low. At higher salinities and recoveries, the reversible work rises more than the irreversible work, increasing the efficiency.

3.2. Multi-Effect Distillation

Multi-Effect Distillation (MED), or Multi-Effect Evaporation (MEE), is a well-established desalination technology that recycles the enthalpy of vaporization in successive effects to achieve a high gained output ratio (GOR). It has been widely deployed in seawater desalination, but is also used at smaller scales to treat industrial and other wastewaters [32]. Its reliability and robustness to fouling make it an attractive option for produced water treatment.

Several configurations of MED exist [33], but we analyze the forward-feed variant here. As shown in Fig. 6, a saline stream warms in a series of feed heaters, and is sprayed over a tube bundle in the first effect, where it is sensibly heated and a portion $(f_1 + F_1)$ vaporizes. The brine from the first effect is then sent to a second effect, where a portion (f_2) flashes and a portion (F_2) is evaporated. The condensation of f_1 in the first feed heater preheats the feed, and the condensation of F_1 in the second effect provides the heat to vaporize F_2. In subsequent effects, the condensation of the vapor flashed in the effect (f_i) and in the flash box (d_i) preheats the feed stream in the feed heaters. This process can be repeated several times, although fewer effects are more common at smaller scales.

Mistry et al. [26] provide a detailed numerical model for MED and benchmark it against several alternatives. For thermodynamic considerations, Mistry et al. [26] find that the analytical model by El-Sayed

[2]Because the work is inversely proportional to compressor efficiency, lower values of η will decrease the system energy efficiency proportionally.

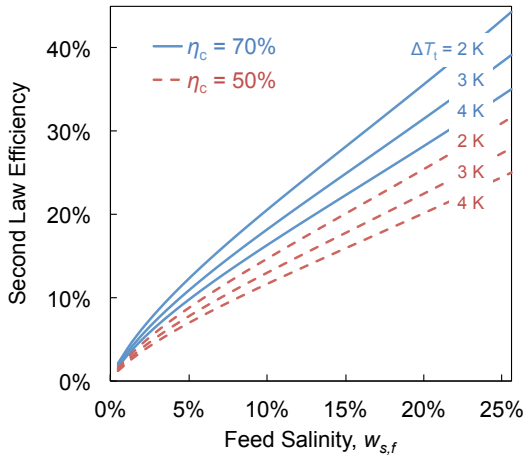

Figure 5: At fixed brine salinity, the energy consumption of MVC is fairly insensitive to changes in feed salinity, so it operates closer to its reversible limit at higher salinities.

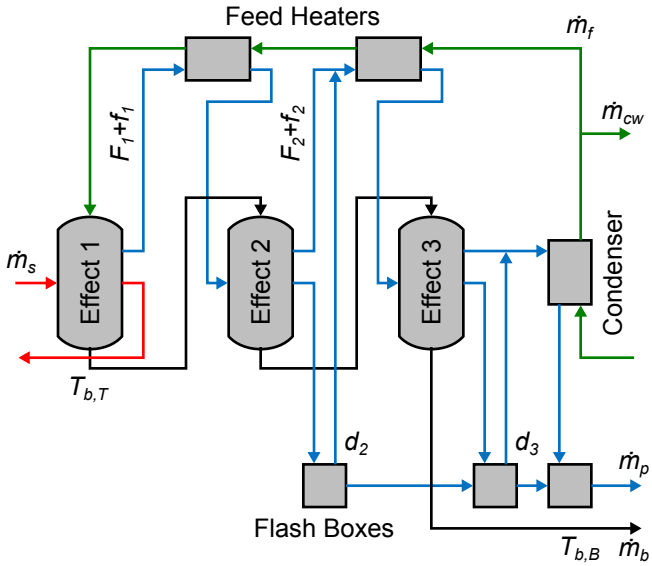

Figure 6: A schematic diagram of a three-effect, forward-feed MED system: the water vaporized in the first effect condenses in the second effect to produce more vapor at a lower pressure; the vapor flashed in each effect condenses in a feed heater to preheat the feed. Depending on the plant, the process is repeated anywhere from three to 15 or more times to obtain better energetic performance.

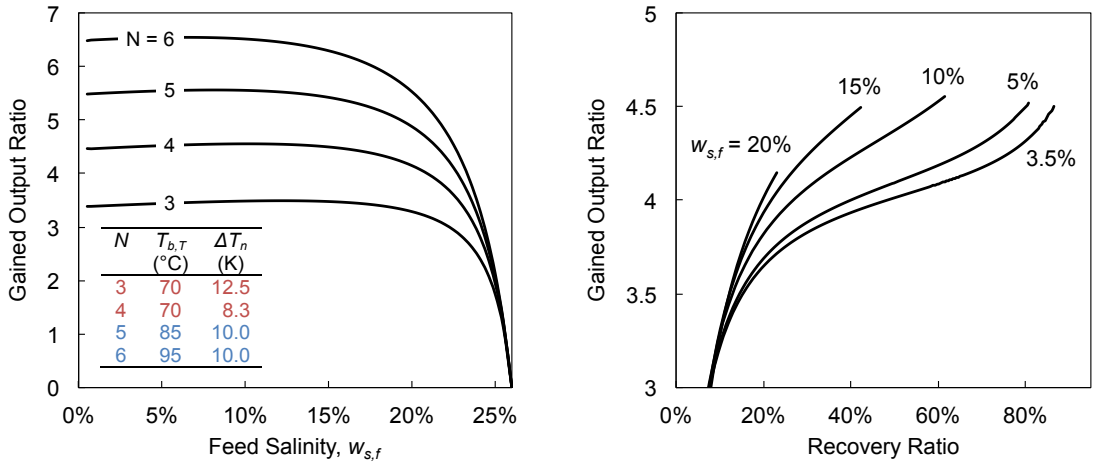

(a) $w_{s,b} = 26\%$ (b) $N = 4$, $T_{b,T} = 70\,^{\circ}\mathrm{C}$

Figure 7: Energetic figures of merit for MED: (a) At fixed brine salinity, GOR increases with the number N of effects and is relatively stable across a broad range of feed salinities, until low recoveries at high feed salinities result in relatively large irreversible heat transfers in the preheat train and reduce GOR. (b) GOR rises with increasing feed salinity and recovery ratio.

and Silver [34] produces results closely in line with the more detailed numerical model. The heat per unit distillate is given by [34] as

$$\frac{\dot{Q}_i}{\dot{m}_p} = \frac{\bar{h}_{fg}}{N} + \frac{\bar{c}_p}{\mathrm{RR}}(\Delta T_t + \bar{\delta}) + \frac{1}{2}\frac{N-1}{N}\bar{c}_p \Delta T_n \tag{16}$$

where $\bar{h}_{fg}$, $\bar{c}_p$, and $\bar{\delta}$ are the average enthalpy of vaporization, liquid specific heat, and boiling point elevation across the effects; ΔT_t is the terminal temperature difference in the feed heaters, and ΔT_n is the stage-wise temperature drop. The stage-wise temperature drop is calculated from a defined top and bottom brine temperature:

$$\Delta T_n = \frac{T_{b,T} - T_{b,B}}{N-1} \tag{17}$$

The driving temperature difference for evaporation in each effect is $\Delta T_n - \delta_n$. Here, we take $T_{b,T} = 70\,^{\circ}\mathrm{C}$ as a baseline value[3] and increase it for higher numbers of effects (Fig. 7a) so that $\Delta T_n - \delta_n$ is not too small. Because δ at high salinities may be comparable to ΔT_t and ΔT_n, $T_{b,B}$ must be chosen high enough that the condenser has a measurable driving temperature difference: $T_{b,B} \geq T_f + \delta_N + \Delta T_t$. We take $T_{b,B} = 45\,^{\circ}\mathrm{C}$, which is slightly higher than typical seawater systems to allow for the higher BPEs. In other sections, ΔT_t was varied to reflect different system scales. Here, the number of effects N, which maps to a driving temperature difference in each effect [Eq. (17)] for a given top and bottom temperature and salinity, is varied to reflect system size. The terminal temperature difference in the feed heaters and condenser is fixed at $\Delta T_t = 4$ K.

As with HDH and PGMD, we report the energy consumption of MED in terms of a gained output ratio, or GOR ($= \dot{m}_p h_{fg}/\dot{Q}_i$), as shown in Fig. 7a. At high recoveries and a small number of effects, most of the vapor produced is by evaporation, so the first term in Eq. (16)—representing the energy recycled within the effects—is dominant. The changes in average latent heat $\bar{h}_{fg}$ and average BPE $\bar{\delta}$ act in opposite directions and are small relative to the effect of N, so GOR appears weakly dependent on feed salinity up to about 15%–20%. At higher feed salinities (i.e., lower recovery), a larger fraction of the vapor is produced by flashing, and the irreversibilities associated with the recycle of that heat (viz. the preheating of the feed)

[3]This value is common in seawater MED systems and is so chosen to limit formation of calcium sulfate scale, which has inverse solubility. Although certain produced water compositions and appropriate pretreatment may remove this upper limit, a higher $T_{b,T}$ in itself only weakly effects energy consumption through the reduction in h_{fg}. Rather, the higher $T_{b,T}$ simply allows for a greater number of effects, which may not be economically advantageous at small scale.

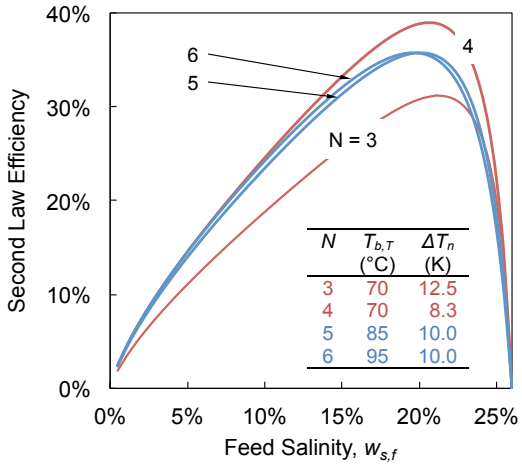

Figure 8: Because the least heat increases with feed salinity, the efficiency peaks around $w_{s,f} = 20\%$. Increasing the number of effects at a fixed top temperature decreases the effective driving force for evaporation and increases the efficiency ($N = 3, 4$); larger N at fixed ΔT_n only marginally raises efficiency, as the least heat decreases at higher top temperature ($N = 5, 6$).

dominate. GOR decreases as an increasingly large mass of feed is irreversibly heated in imbalanced feed heaters to produce an increasingly smaller amount of product. As N increases, the energy producing vapor by evaporation is increasingly reused, and the irreversibilities in the preheat train become more relevant at lower feed salinities.

At fixed brine salinity, because the least heat rises with feed salinity, the net effect on efficiency is a peak around $w_{s,f} = 20\%$ (Fig. 8). Higher numbers of effects at a fixed top temperature decrease the driving force for evaporation within an effect, resulting in an increased efficiency. However, a similarly sized system with the same ΔT_n but an increased $T_{b,T}$ results in only a modest improvement in efficiency, as the least heat decreases at higher top temperatures.

Two major effects of higher salinity on energy consumption influence system design. First, the higher BPE in the feed heaters acts as an effective increase in ΔT_t, limiting the preheat and thus requiring a greater heat input in the first effect. When feed salinities are high and recoveries are low, it is thus worth considering multistage flash (MSF) as an alternative to MED. Because a smaller fraction of the distillate is produced by evaporation, the cost of the additional hardware for falling film evaporation within an effect may not be advantageous compared to the cost of the smaller but more numerous stages required for MSF.

Second, for a fixed top temperature, a higher BPE also limits the number of effects, as it decreases the driving force for evaporation within an effect. This essentially implies that higher salinity MED systems will operate with greater temperature differences between effects. A sufficiently pretreated feed that allows for a higher $T_{b,T}$ would reduce the average $\bar{h}_{fg}$ and allow for more effects, both of which increase GOR. However, as the number of effects increases, so do capital expenditures, which may not be favorable at the relatively smaller system sizes found in produced water treatment.

3.3. Forward Osmosis

Produced water remediation is among the most promising applications of forward osmosis (FO) [35]. FO with thermal draw regeneration can operate at high salinities beyond the reach of RO [36], and FO exhibits more easily reversible fouling compared to RO [37], which is an advantage when treating complex waters.

In forward osmosis, as in Fig. 9, a concentrated solution with a high osmotic pressure draws water from a saline feed by osmosis, concentrating the feed stream and diluting the draw stream. The draw solution is then regenerated through a separation of the diluted draw (dd) into permeate (p) and concentrated draw (dc). For high-salinity produced water applications, thermal regeneration is necessary due to the high draw solution osmotic pressures. The FO process with thermal regeneration has been demonstrated treating water from the Marcellus and Permian Basin shale regions [36]. This pilot uses an ammonia-carbon dioxide draw solution which can reach high osmotic pressures, enabling concentration of the produced water to

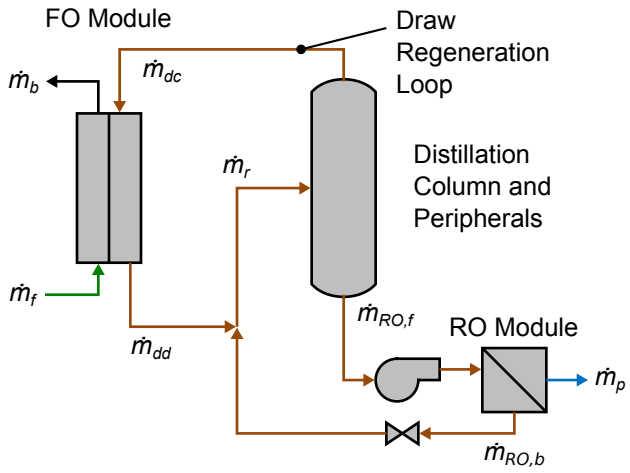

Figure 9: Schematic diagram of FO with thermal draw regeneration: water drawn from a saline feed dilutes a high osmotic pressure draw solution in the FO module. The draw solution is then reconcentrated in a distillation column and small RO unit, producing pure water.

saturation. The solubility of the gases in the liquid decreases with temperature, enabling regeneration by a simple distillation column.

Models exist for the energy consumption of FO seawater desalination with thermal regeneration [38, 39], but a more general model is needed to extend these predictions to produced water. The model presented here is developed for a system similar to that used in [36], with the same ammonia-carbon dioxide draw solution and with regeneration efficiency benchmarked against data from the pilot plant.

The model system is depicted schematically in Fig. 9. Produced water concentration occurs in a counter-flow FO unit. The draw solution is regenerated in a generic distillation unit, such as a stripping column and peripherals. As in [36], the dilute bottoms product of the distillation column is treated with RO to remove the remaining solutes. The RO concentrate, which is dilute compared to the draw streams, is returned to the diluted draw stream rather than the concentrated draw stream to minimize entropy generation. Circulation pumps are neglected in the model because of their minimal contribution to energy consumption. Not modeled are any additional steps that may be needed to remove aqueous ammonia from the permeate [38].

Draw solution properties were modeled using the extended UNIQUAC model [40] with additional parameters from [41]. All draw streams were modeled as having a total nitrogen to carbon mole ratio of 2.4. The solid-liquid-vapor equilibrium model shows that at 25 °C the osmotic pressure of this solution can climb above 500 bar.

The feed salinity is an input to the model, and saturated brine ($w_{s,b} = w_s^s$) and pure permeate ($w_{s,p} = w_{d,p} = 0$) are assumed. Assuming a temperature of 80 °C and a pressure of 1 atm in the distillation column reboiler, we model the bottoms product (and the feed to the RO) as having a total draw solute mass fraction of $w_{d,RO,f} = 0.0137$. To reduce the fraction of brine that must be recirculated, the RO unit should operate at high recovery. The RO unit is therefore operated at a typical SWRO operating pressure, P_{RO}, of 70 bar with a typical terminal pressure pinch, ΔP_t, of 10 bar. The osmotic pressure of the RO brine is then $\Pi_{RO,b} = P_{RO} - \Delta P_t$, leading to an RO brine draw solute mass fraction that has the correct osmotic pressure, $w_{d,RO,b} = w_{d,d}|_{\Pi_{RO,b}}$.

Concentrated (dc) and dilute (dd) draw mass fractions are chosen by offsetting feed and brine osmotic pressures with a fixed terminal osmotic pressure pinch, $\Delta\Pi_t$, estimated from [36] as 57 bar, resulting in $w_{d,dc} = w_d|_{\Pi_c+\Delta\Pi_t}$ and $w_{d,dd} = w_d|_{\Pi_f+\Delta\Pi_t}$. Examples of FO exchanger salinity profiles can be seen in [42]. Thermodynamically balancing the FO exchanger by setting the osmotic pressure pinch equal on feed and brine ends maximizes system efficiency when the draw regeneration efficiency is roughly independent of salinity [42], as it is in this model. Mass and species conservation in the FO exchanger leads to Eq. (18) for

the mass flow rate ratio (draw to feed) needed to maintain the desired draw salinities:

$$\frac{\dot{m}_{dc}}{\dot{m}_f} = \frac{w_{d,dd}}{w_{d,dc} - w_{d,dd}} \frac{w_{s,f} - w_{s,b}}{w_{s,b}}. \tag{18}$$

Mass and solute balances throughout the system, neglecting salt permeation through FO and RO membranes, lead to an expression for the draw solute mass fraction that is fed to the regenerator:

$$w_{d,r} = \frac{\dfrac{w_{d,dc} w_{d,dd}}{w_{d,dc} - w_{d,dd}} + \dfrac{w_{d,RO,f} w_{d,RO,b}}{w_{d,RO,b} - w_{d,RO,f}}}{\dfrac{w_{d,dc}}{w_{d,dc} - w_{d,dd}} + \dfrac{w_{d,RO,f}}{w_{d,RO,b} - w_{d,RO,f}}}. \tag{19}$$

The RO unit is operated at a very high recovery ratio (>80%), which shifts economic favor away from the use of an energy recovery device. In the absence of energy recovery and assuming 85% pump efficiency (η_p), the RO unit power is

$$\dot{W}_{RO} = \frac{\dot{m}_{RO,f} P_{RO}}{\eta_P \rho_p} = \frac{\dot{m}_p P_{RO}}{\eta_P \rho_p} \frac{w_{d,RO,b}}{w_{d,RO,b} - w_{d,RO,f}}, \tag{20}$$

with the conservative approximation that the low-salinity RO feed has the same density, ρ, as pure water.

The FO unit requires a small amount of work to drive flow through the channels, but the hydraulic pressure drop (less than 2.8 bar in a pilot study [36]) is very small compared to the osmotic pressures involved, so the parasitic work consumption of the FO exchanger is neglected in the present analysis.

Equation (21) shows that the regenerator exergy input is related by an efficiency [43] to the change in Gibbs energy (g) of the distillation column's incoming and outgoing streams, evaluated as liquids at 25 °C and 1 atm:

$$\dot{\Xi}_r = \frac{1}{\eta_r} [\dot{m}_{dc} g_d|_{w_{d,dc}} + \dot{m}_{RO,f} g_d|_{w_{d,RO,f}} - \dot{m}_r g_d|_{w_{d,r}}]. \tag{21}$$

Although distillation column efficiency will vary somewhat with feed and distillate salinity, a fixed distillation column exergetic efficiency of 8.3% was assumed based on the reported heat consumption of [36]. The exergy input to the regenerator, $\dot{\Xi}_r$, will depend on the type of distillation used and can be any combination of work, heat, and fuel.

Using Eqs. (20) and (21) along with mass and salt balances, we arrive at Eq. (22) for the total exergy consumption:

$$\frac{\dot{\Xi}}{\dot{m}_p} = \frac{1}{\eta_r} \left(\frac{w_{d,dd}}{w_{d,dc} - w_{d,dd}} [g_d|_{w_{d,dc}} - g_d|_{w_{d,r}}] \right. \tag{22}$$

$$\left. + \frac{w_{d,RO,b}}{w_{d,RO,b} - w_{d,RO,f}} [g_d|_{w_{d,RO,f}} - g_d|_{w_{d,r}}] \right) + \frac{P_{RO}}{\eta_P \rho_p} \frac{w_{d,RO,b}}{w_{d,RO,b} - w_{d,RO,f}}. \tag{23}$$

Equation (19) can be used to calculate the mass fraction at the regenerator inlet, $w_{d,r}$.

Equation (22) can be used in conjunction with the least work (Eq. (6)) to estimate the exergy consumption and efficiency of treating produced water to saturation with FO. In addition to the system parameters derived from [36], the effects of halving the osmotic pressure pinch to 28.5 bar and doubling the regenerator efficiency to 17% are calculated.

The energy consumed in concentrating a feed to saturation is shown in Fig. 10. The energy consumption increases strongly with increasing feed salinity, as is typical of membrane processes. The second-law efficiency, shown in Fig. 11, increases with feed salinity until reaching a plateau around 6.5%.

FO is an emerging technology that has not yet been optimized. FO is attractive for its fouling resistance and waste heat compatibility, but comparison to the efficiency of other processes discussed in this paper suggests that efficiency improvement is necessary if FO is to be *energetically* competitive for produced water treatment. Figure 11 also shows that improving the distillation column efficiency has a much more significant impact than reducing the FO unit's osmotic pressure pinch. Efficiency improvement may come through

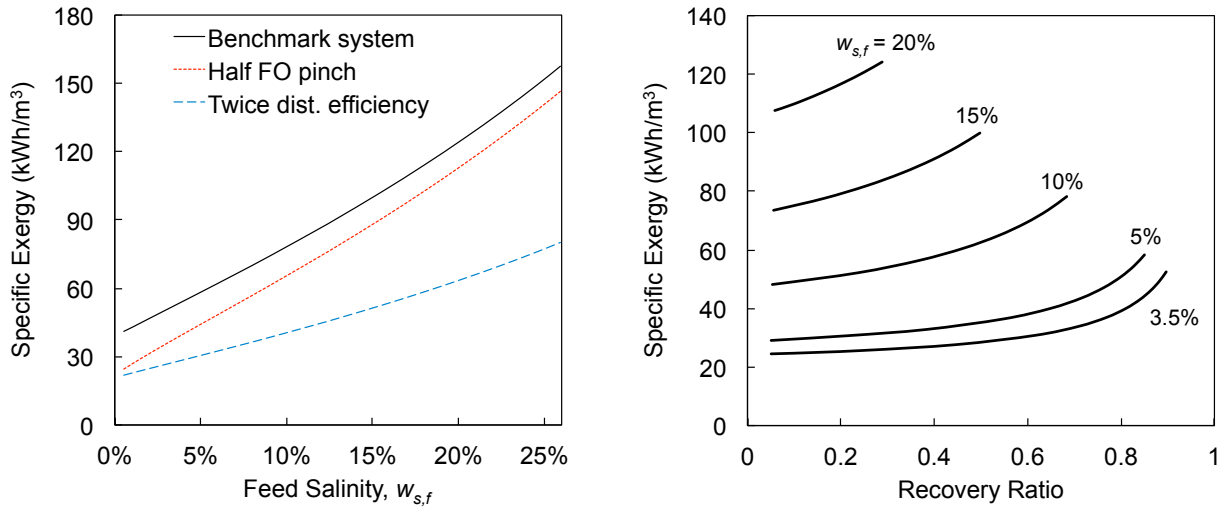

(a) $w_{s,b} = 26\%$ (b) $\eta_r = 8.3\%$

Figure 10: (a) Exergy consumption of concentration to saturation with FO, showing that exergy consumption increases with feed salinity. Benchmark system uses an FO terminal osmotic pressure pinch and distillation column efficiency calculated from pilot plant data [36]. (b) Exergy consumption as a function of recovery for several feed salinities.

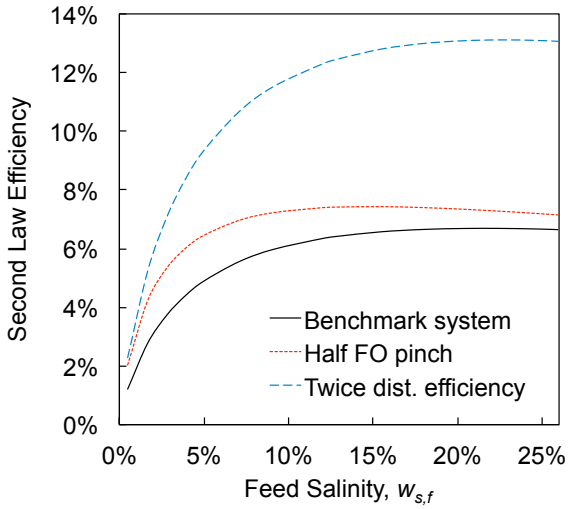

Figure 11: Exergetic efficiency of the model FO system concentrating a range of feed salinities to saturation, showing best performance at high salinities. Benchmark system uses FO osmotic pressure pinch and distillation column efficiency calculated from pilot plant data [36]. Efficiency can be improved significantly by raising the distillation column efficiency.

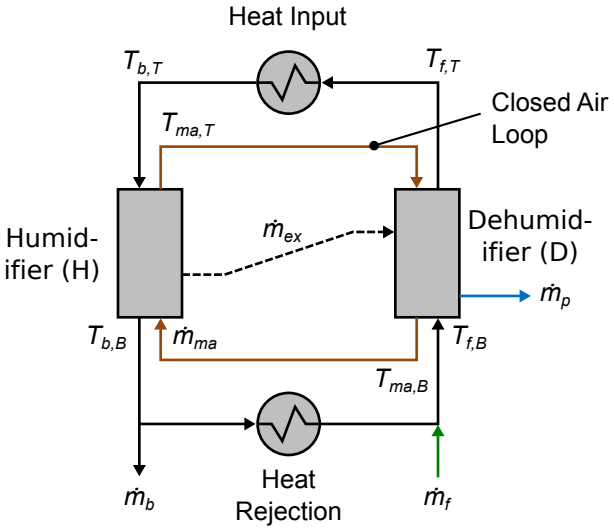

Figure 12: Schematic diagram of a typical HDH system: a closed air loop evaporates pure vapor from a saline stream in the humidifier and condenses it in the dehumidifier, producing fresh water. Cycle variants exist with and without an extraction (dashed line), which can help to balance the humidifer and/or dehumidifier.

the use of advanced draw regeneration processes such as mechanical vapor compression [36],[4] membrane distillation [44], or multi-stage flash distillation [45] rather than an isobaric distillation column. However, due to the unique properties of the draw solution, the optimal draw regeneration technology may be something other than an established desalination process.

3.4. Humidification-Dehumidification

Humidification-dehumidification (HDH) is an emerging desalination technology that uses a carrier gas to separate water vapor from a saline water stream at low temperatures. The equipment is robust and has been demonstrated in the treatment of produced water from the Permain Basin [17].

A schematic diagram of a typical HDH system is shown in Fig. 12. In the humidifier, pure vapor evaporates from a warm, saline feed to humidify a moist air stream. The warm, moist air leaves the humidifier at $T_{ma,T}$ and condenses in the dehumidifier, producing a pure water stream. Cooling in the dehumidifier is provided by the saline feedwater, which is preheated from $T_{f,B}$ to $T_{b,T}$ as the moist air stream dehumidifies. The preheated feed is sent to a water heater where the heat input to the cycle is provided, raising the feed to the top brine temperature, $T_{b,T}$. Because the system is inherently low recovery in a single pass, the brine leaving the humidifier is generally recirculated in brine concentration applications. This requires a heat rejection step at the bottom of the cycle so that the temperature of the recirculated brine is reduced to $T_{f,B}$.

In recent years, several improvements to the HDH system have been proposed in literature. For example, the humidifier and dehumidifier may both be multistage bubble columns [46, 47], which have much lower heat and mass transfer resistances [48] than packed beds or indirect contact heat exchangers. The extraction and injection of water or air from one component to the other in order to balance the humidifier or dehumidifier and increase energy efficiency has also been investigated [49–53]. For the purposes of this analysis, which is to show the effect of high salinity on energy consumption and efficiency, the thermodynamic investigation of the zero extraction cycle is sufficient; research on the high-salinity single- and multi-extraction variants is ongoing. We will build on the approach of McGovern et al. [51], who use enthalpy-temperature diagrams to visualize water and moist air process paths in the humidifer and dehumidifier, as this graphical approach

[4]McGinnis et al. [36] model FO with MVC-like regeneration using Aspen Plus and claim that it can be more efficient than MVC alone, but this result has yet to be conceptually explained or supported by data.

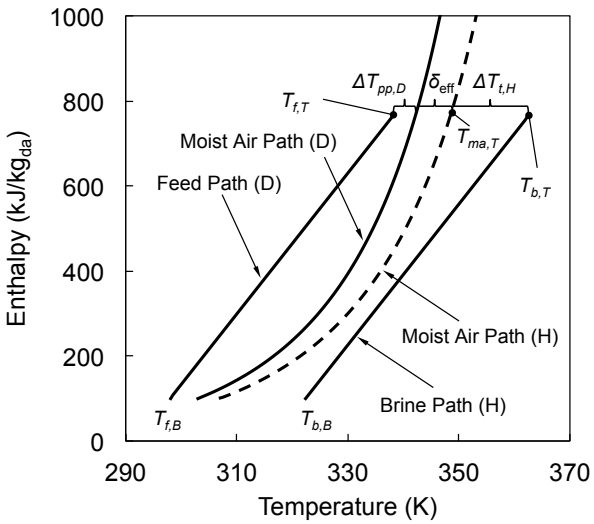

Figure 13: Process paths of feed, brine, and air streams on a zero extraction HDH system on an enthalpy-temperature diagram: the top and bottom air temperatures are 70 °C and 25 °C, respectively.

proves to build intuition on salinity effects. The key modeling approximation in this approach is to treat the air as saturated in the humidifier and dehumidifier, which provides a well-defined process path for all streams. For feeds at oceanographic salinities or below, McGovern et al. [51] have shown that using pure water properties introduces an error of no more than 4–5%. We will drop this assumption, as the salinities encountered in brine concentration are significantly higher.

The general process for analyzing the HDH system using a saturation curve (enthalpy-temperature, Fig. 13) approach is as follows. The top and bottom moist air temperatures $T_{ma,T}$ and $T_{ma,B}$ are chosen, which specifies the process path of the moist air. The mass flow rate ratio (MR) in the dehumidifier is chosen such that the pinch point temperature differences (ΔT_{pp}) in the dehumidifier are equal at both ends. This defines the feed process path in the dehumidifier. The ΔT_{pp} in the humidifier is then chosen; with the mass flow rate ratio, ΔT_{pp}, and top air temperature fixed, the brine process path in the humdifier is completely defined by energy conservation. The details of these steps at high salinities for a zero extraction cycle are below.

Salinity effects appear in the calculation of energy consumption in two ways: the reduction in specific heat of the saline streams and the vapor pressure depression in the humidifier. To construct the enthalpy-temperature diagram showing the process paths (Fig. 13), we thus require two saturation curves: one for the dehumidifier (moist air in contact with pure water), and one for the humidifier (moist air in contact with saline water). The enthalpy of saturated moist air per kg of dry air is

$$h^s_{ma} = h_{da} + \omega^s h^s_v \tag{24}$$

where h is enthalpy, the subscripts ma, da, and v indicate moist air, dry air, and water vapor, respectively, and the superscript s denotes a saturated state. The saturated humidity ratio of moist air is

$$\omega^s = \frac{M_w}{M_{da}} \frac{a_w P^s}{P - a_w P^s} \tag{25}$$

where M is molar mass, and a_w is the activity of the liquid water in contact with the moist air. In the dehumidifier, the liquid condensing is pure water, so $a_w = 1$; in the humidifier, the liquid phase is an aqueous NaCl solution, and $a_w < 1$. Because the brine is recirculated, the single pass recovery ratio is low, and the brine salinity is fixed, the saturation curve in the humidifier is approximately fixed at the brine salinity. The difference in temperature between a pure and saline solution at the same humidity ratio (i.e., the same vapor pressure) is the boiling point elevation (BPE). As shown in Appendix A.2, the difference in temperature between a pure and saline solution at the same enthalpy is not quite the BPE owing to sensible

heat contributions from h_{da} and h_v at different temperatures; we denote this temperature difference as the effective BPE, δ_{eff}. Values of δ_{eff} are tabulated in Appendix A.2. The two saturation curves, labeled as 'Moist Air Path (D)' and 'Moist Air Path (H)', are shown in enthalpy-temperature space in Fig. 13.

The dehumidifer process path is set by an energy balance on the dehumidifier, requiring an equal ΔT_{pp} (pinch point temperature difference) at both ends of the dehumidifier. Solving the enthalpy balance for the mass flow rate ratio, $\text{MR} = \dot{m}_f/\dot{m}_{da}$, yields[5]

$$\text{MR} = \frac{(h_{ma,T} - h_{ma,B}) - (\omega_T^s - \omega_B^s)h_p}{c_{p,f}(T_{ma,T} - \delta_{\text{eff}} - \Delta T_{pp} - T_{f,B})} \approx \frac{(\omega_T^s - \omega_B^s)h_{fg}}{c_{p,f}(T_{ma,T} - \delta_{\text{eff}} - \Delta T_{pp} - T_{f,B})} \tag{26}$$

The feed is preheated to $T_{f,T} = T_{ma,T} - \delta_{\text{eff}} - \Delta T_{pp}$. As the slope of the dehumidifier operating line is $c_{p,f}\text{MR}$ on an enthalpy-temperature diagram, knowledge of MR, $T_{f,B}$, and $T_{f,T}$ allows us to draw the dehumidifier process path (or 'Feed Path (D)') shown in Fig. 13.

With MR defined, the slope of the humidifier operating line is also well defined. The top brine temperature in the humidifier is found by drawing a line with slope $c_{p,b}\text{MR}$ up from the pinch point in the humidifier. This line is defined by an energy balance on the humidifier between the pinch point and the top of the humidifier. The pinch point is where the slope of the humidifier saturation curve equals the slope of the brine stream line, as defined by an enthalpy balance on a small slice of the humidifier at the pinch point:

$$c_{p,b}\left[\text{MR} - (\omega_T^s - \omega_{pp,H}^s)\right] = c_{p,da} + \omega c_{p,v} + h_{fg,b}\frac{d\omega^s}{dT} \approx h_{fg,b}\frac{d\omega^s}{dT} \tag{27}$$

where $h_{fg,b}$ is the enthalpy of vaporization of water from the brine stream. In order to evaluate $d\omega^s/dT$, we make two further approximations: the small temperature dependence of a_w is neglected, and the Clausius-Clapeyron equation with the usual ideal gas approximation is used for the slope of the pure water saturation curve. Carrying out the differentiation, we find

$$\frac{d\omega^s}{dT} = \frac{M_w^2}{M_{da}}\frac{h_{fg}}{RT^2}\frac{a_w P P^s}{(P - a_w P^s)^2} \tag{28}$$

Thus, substituting Eq. (28) into (27), the temperature of the moist air at the pinch point in the humidifier, $T_{ma,pp,H}$, satisfies

$$c_{p,b}\left[\text{MR} - (\omega_T^s - \omega_{pp,H}^s)\right] = c_{p,da} + \omega c_{p,v} + h_{fg,b}\frac{M_w^2}{M_{da}}\frac{h_{fg}}{RT_{ma,pp,H}^2}\frac{a_w P P^s}{(P - a_w P^s)^2} \tag{29}$$

Because $P^s = f(T_{ma,pp,H})$, this equation must be solved numerically with an appropriate expression for the vapor pressure curve [54].

With $T_{ma,pp,H}$ obtained from Eq. (29), energy conservation on the upper half of the humidifier allows us to solve for the top brine temperature:

$$\begin{aligned} T_{b,T} &= T_{ma,pp,H} + \Delta T_{pp} + \frac{(h_{ma,T} - h_{ma,pp,H}) - (\omega_T^s - \omega_{pp,H}^s)h_{b,pp,H}}{c_{p,b}\,\text{MR}} \\ &\approx T_{ma,pp,H} + \Delta T_{pp} + \frac{(\omega_T^s - \omega_{pp,H}^s)h_{fg,b}}{c_{p,b}\,\text{MR}} \end{aligned} \tag{30}$$

Finally then, the heat input per unit water produced is

$$\frac{\dot{Q}_i}{\dot{m}_p} = c_{p,f}\,\text{MR}\left(\frac{T_{b,T} - T_{ma,T} + \Delta T_{pp} + \delta_{\text{eff}}}{\omega_T^s - \omega_B^s}\right) \tag{31}$$

which is often reported as a gained output ratio[6], $\text{GOR} = \dot{m}_p h_{fg}/\dot{Q}_i$.

[5] Neglecting the sensible heat components of the moist air enthalpy change allows the equations required to construct the enthalpy-temperature diagram to be simplified considerably, as shown by the approximation in Eq. (26). However, this approximation may induce errors up to about 10% in the final values of energy consumption.

[6] For the reasons detailed in [51], we evaluate h_{fg} in the calculation of GOR at ambient temperature, 25 °C.

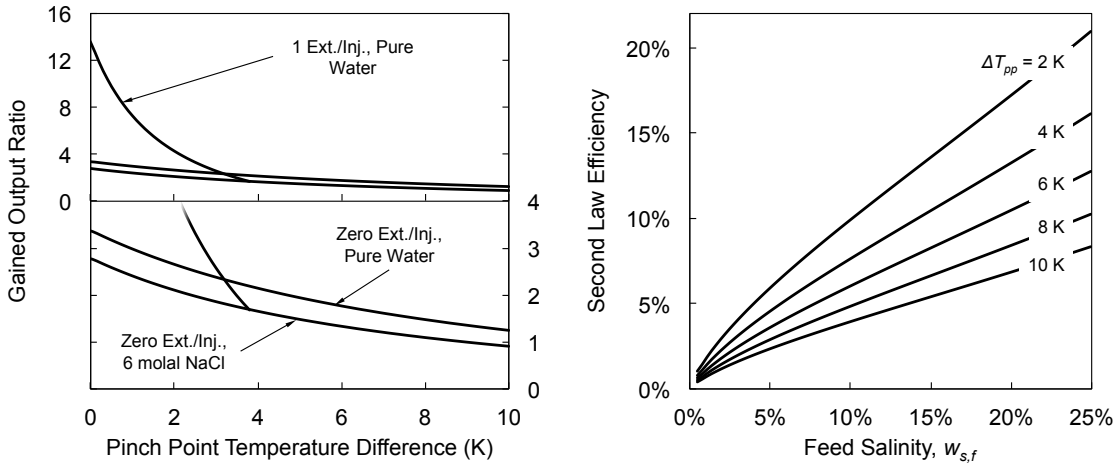

(a) $T_{ma,T} = 70\,^{\circ}\mathrm{C}$, $T_{f,B} = 25\,^{\circ}\mathrm{C}$ (b) $T_{ma,T} = 70\,^{\circ}\mathrm{C}$, $T_{f,B} = 25\,^{\circ}\mathrm{C}$

Figure 14: Energetic figures of merit for HDH over the salinity domain: (a) GOR, benchmarked against zero salinity data from [51], and (b) efficiency. Because HDH is inherently low recovery in a single pass, the brine recirculation configuration required for high recovery wastewater treatment means that the system always operates at the highest (brine) salinity, and has energy consumption that is insensitive to feed salinity.

The GOR for the HDH system at high salinity versus ΔT_{pp} is shown in Fig. 14a, benchmarked against the zero and single extraction cases at zero salinity from McGovern et al. [51]. In the high salinity, zero extraction case, GOR is reduced by about 17–27% relative to the zero salinity, zero extraction case. Owing to the effective boiling point elevation, the temperature to which the feed can be preheated is limited, resulting in a greater required heat input. In addition, because of the vapor pressure depression, the highest humidity ratio for air in contact with a saline stream at $T_{ma,T}$ is lower than for air in contact with a pure water stream at the same temperature. The recovery ratio (in a single pass) for a system operating between the same top and bottom air temperatures is thus reduced. The reduced water production and the limited preheat both reduce GOR.

The second law efficiency is shown in Fig. 14b, where the curves tend to increase with increasing feed salinity. The low recovery for a single pass of feed through the HDH system forces brine recirculation for wastewater concentration applications so that the system effectively always operates at the brine salinity. Thus, when the desired brine concentration is high, the thermal energy consumption of HDH is truly feed-salinity invariant. As a result, because the least work is higher at higher feed salinities, the system is operating closer to its reversible limit.

3.5. Membrane Distillation

Membrane distillation is an emerging desalination technology that uses a vapor pressure difference across a membrane that selectively admits water vapor, but rejects the liquid phase. Several variants of the technology exist, and although direct contact membrane distillation (DCMD) has been examined for produced water applications in the past [14, 55], we choose to evaluate permeate gap membrane distillation (PGMD) here. PGMD is a variation on direct contact membrane distillation (DCMD) that integrates energy recovery directly into the membrane module, eliminating the need for an additional external heat exchanger. Unlike air gap membrane distillation (AGMD) [56], which also integrates energy recovery into the membrane module, the air-gap is eliminated, reducing the mass transfer resistance between the cold side of the membrane surface and the permeate stream.

A schematic diagram of a PGMD system is shown in Fig. 15. Feed enters the membrane module and is heated to a top temperature ($T_{f,T}$). The hot feed enters an evaporator, where it passes over a hydrophobic membrane that is permeable to water vapor, but rejects the liquid phase. The cold side of the membrane is in contact with the permeate stream. The temperature difference across the membrane creates a vapor pressure difference, driving evaporation on the hot side of the membrane and condensation on the cold side. In PGMD, heat is transferred through the permeate and into the feed stream to provide the preheat.

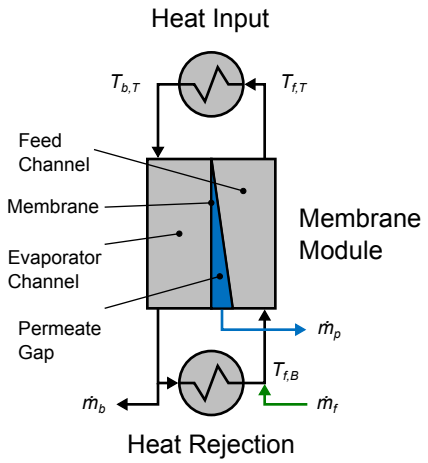

Figure 15: Schematic diagram of a PGMD system: a vapor pressure difference across a hydrophobic membrane that selectively admits water vapor drives evaporation in the evaporator and condensation in the permeate gap, producing desalinated water.

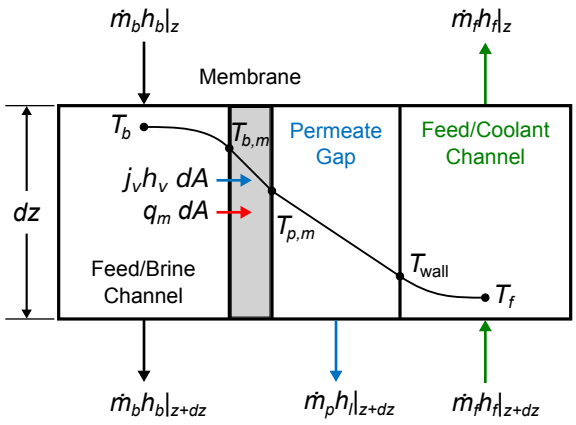

Figure 16: Differential control volume used in the PGMD model

The modeling approach used here is based on the finite difference method of Summers et al. [57], with two major differences. First, whereas Summers et al. used pure water properties, NaCl solution properties are used here. Second, Summers et al. modeled AGMD; in PGMD the air gap is eliminated, and the condensate film completely fills the permeate channel. A summary of the approach follows; more details can be found in [57].

A flat sheet-type PGMD module was divided into finite segments as shown in Fig. 16. With the feed inlet ($T_{f,B}$) and top temperatures ($T_{f,T}$) specified, energy and mass balances, combined with transport equations describing the heat and mass flux across the membrane comprise a complete set of equations to solve for the enthalpy and mass flow rates at each node. Owing to the high convective heat transfer coefficient in both feed and cooling channels, the temperature difference across the channels is negligible. The equations were solved in an iterative manner using the bisection method.

The permeate flux was calculated as

$$J = B(P_{b,m} - P_{p,m}) \tag{32}$$

where B is the membrane distillation coefficient. The membrane represented by this model is a commercial Durapore membrane manufactured by Millipore, which has a membrane distillation coefficient of $B = 16.2 \times$

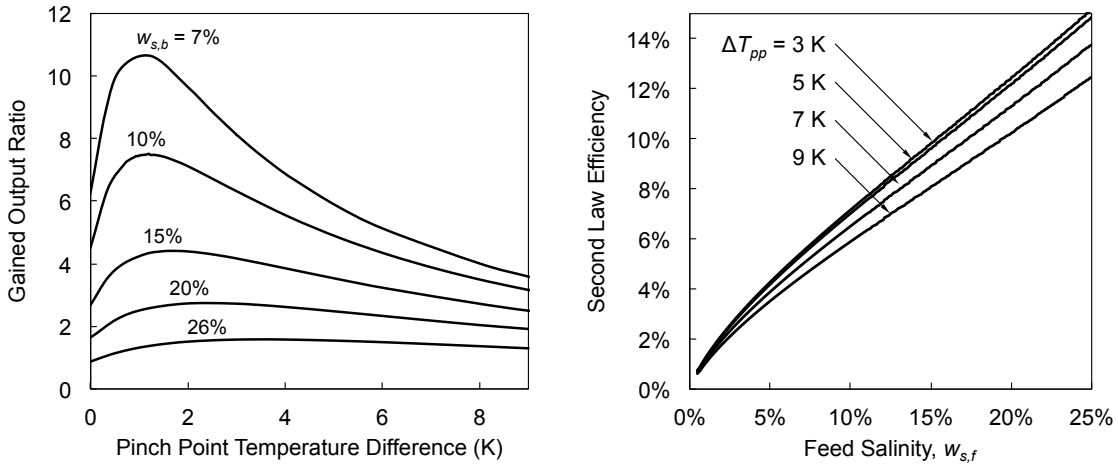

(a) $T_{b,T} = 80\,^{\circ}\text{C}$, $T_{f,B} = 25\,^{\circ}\text{C}$ (b) $T_{b,T} = 80\,^{\circ}\text{C}$, $T_{f,B} = 25\,^{\circ}\text{C}$

Figure 17: Energetic figures of merit for PGMD: (a) GOR at several brine salinities and (b) efficiency at 26% brine salinity.

10^{-7} kg/m^2-s-Pa [57]. Feed inlet and top brine temperature are $T_{f,B} = 25\,^{\circ}\text{C}$ and $T_{b,T} = 80\,^{\circ}\text{C}$, respectively.

Unlike pure heat exchangers where a zero pinch point temperature difference (ΔT_{pp}) corresponds to an infinite size, at non-zero salinity, there exists a finite minimum ΔT_{pp} in MD when the permeate flux is zero, defined as follows:

$$\Delta T_{pp,\min} = \lim_{J \to 0} (T_{b,T} - T_{f,T}) \tag{33}$$

The difference is finite because of the vapor pressure depression at nonzero salinity. For high salinity applications such as produced water treatment, the vapor pressure depression is quite significant. Therefore, we define the ΔT_{pp} in MD relative to this finite minimum as

$$\Delta T_{pp} = \Delta T_{pp,\text{actual}} - \Delta T_{pp,\min} \tag{34}$$

At $w_{s,b} = 26\%$, $T_{f,B} = 25\,^{\circ}\text{C}$, and $T_{b,T} = 80\,^{\circ}\text{C}$, $\Delta T_{pp,\min}$ was found to be $9.78\,^{\circ}\text{C}$.

Figure 17a shows numerical modeling results for GOR as a function of ΔT_{pp}. When ΔT_{pp} is lower than some critical value (e.g., about 2 K for $w_{s,b} = 26\%$), GOR decreases even though the temperature difference between the streams is smaller. Around the maximum, when ΔT_{pp} is reduced, two effects compete: decreased heat input due to better energy recycling (i.e., $T_{f,T}$ is higher) and reduced flux. Assuming the specific heat capacity does not change much with temperature, heat input decreases linearly with increased $T_{f,T}$. In MD, the flux is driven by a vapor pressure difference; vapor pressure increases exponentially with temperature. When the flux-driving temperature is sufficiently high, e.g. $\Delta T_{pp} = 9$ K, the exponential dependence of vapor pressure amplifies the flux-driving potential. However, when the flux-driving temperature difference becomes extremely small, e.g. $\Delta T_{pp} = 1$ K, this amplification effect virtually vanishes, reducing permeate flux significantly. When the permeate flux is lowered, the specific heat input, defined as $Q_i/\dot{m}_p$, becomes large. Since both GOR and second law efficiency are inversely proportional to specific heat input, the performance of PGMD is reduced when ΔT_{pp} decreases below a critical value.

Figure 17b shows the second law efficiency as a function of inlet feed salinity for different ΔT_{pp} values. Like HDH, MD has a low recovery in a single pass, and brine recirculation is required. Therefore, just as for HDH, the energy consumption in MD is practically independent of feed salinity. Because of the strong variation of least work with salinity, the efficiency increases with feed salinity.

3.6. Hypothetical High Salinity Reverse Osmosis

Although reverse osmosis (RO) has been used to treat lower salinity produced waters from coal bed methane production [58], it is unproven at salinities higher than about 7%. (Some challenges associated with developing a high salinity RO system are discussed in Appendix D.) In this section, however, we seek to predict the energetic performance of RO if it were developed to treat the high salinity feed waters encountered

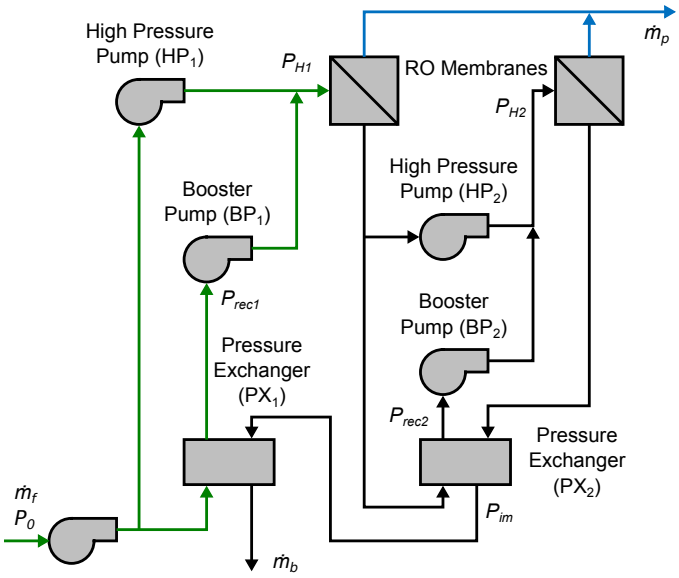

Figure 18: Schematic diagram of a typical two-stage reverse osmosis unit: a pressurized feed stream flows across a semipermeable membrane that selectively admits pure water; energy is recovered from the resulting concentrated brine as it depressurizes in the pressure exchangers.

in shale gas extraction. To do this, we develop a simple thermodynamic model of a two-stage RO system with mechanical energy recovery. Other two-stage RO systems have been investigated in the literature but did not consider energy recovery or high salinity feed streams [59, 60]. A two-stage system is used in the current analysis because it is more energy efficient than a single stage.

The two-stage RO system is shown schematically in Fig. 18. The produced water feed stream enters the low pressure (LP) pump at atmospheric pressure where it is pumped to 2 bar. A portion of the feed is routed to the first high pressure (HP_1) pump where it is brought to the first stage top pressure (P_{H_1}) before entering the first RO stage. Permeate is produced while the feed is concentrated along the length of the membrane and exits as an intermediate brine at a slightly lower pressure (P_{ib}) due to hydraulic losses. Like the feed in the first stage, the intermediate brine is split and a portion is routed to the second high pressure pump (HP_2) where it is pumped to the second stage top pressure (P_{H_2}) before entering the second RO unit. The resulting brine enters two pressure exchangers (PX) which allow for the exchange of mechanical energy with a portion of the intermediate brine and the system feed ($\dot{m}_f$). The intermediate pressure between the PXs can be controlled by a valve. After the PXs, the feed and intermediate brine require booster pumps (BP_1 and BP_2) to reach the top pressure at each stage.

The work input at each pump is

$$\dot{W} = \frac{1}{\eta_p} \frac{\dot{m}(P_o - P_i)}{\rho} \tag{35}$$

where η_p is the pump efficiency, which we take as 80%.

The top pressure required for each stage must be greater than the osmotic pressure of the brine in the last section of the membrane and can be calculated by

$$P_{H_1} = \Delta P_t + \Delta P_{\text{loss}} + \Pi_{ib} \tag{36}$$

$$P_{H_2} = \Delta P_t + \Delta P_{\text{loss}} + \Pi_b \tag{37}$$

where the terminal hydraulic-osmotic pressure pinch (ΔP_t) is reflective of the physical extent of the membrane in much the same way that a terminal temperature difference reflects the size of a heat exchanger. The term ΔP_{loss} represents the extra work required to overcome viscous losses in each stage. The osmotic pressure of the intermediate and final brine Π_{ib} and Π_b is calculated using Eq. 4.

The recovered pressures (P_{rec_1} and P_{rec_2}) in stages 1 and 2 are determined by modeling the PX as an isentropic depressurization-pressurization process, derated by the PX efficiency, η_{PX} [30] (Eqs. (38) and (39)).

We take $\eta_{PX} = 96\%$, as in [30]. Although the PX requires equal volume flow rates of high and low pressure streams for operation, we use the simplifying approximation of equal mass flow rates.

$$P_{\mathrm{rec}_1} = 2\ \mathrm{bar} + \eta_{PX}\frac{\rho_f}{\rho_b}(P_{im} - 2\ \mathrm{bar}) \tag{38}$$

$$P_{\mathrm{rec}_2} = P_{ib} + \eta_{PX}\frac{\rho_{ib}}{\rho_b}(P_b - P_{im}) \tag{39}$$

where $P_{ib} = P_{H_1} - \Delta P_{\mathrm{loss}}$ and $P_b = P_{H_2} - \Delta P_{\mathrm{loss}}$.

In order to express the specific work ($\dot{W}/\dot{m}_p$) more compactly, we introduce several dimensionless parameters. Two recovery ratios for each exchanger

$$\mathrm{RR}_1 = \frac{\dot{m}_{p_1}}{\dot{m}_f} \tag{40}$$

$$\mathrm{RR}_2 = \frac{\dot{m}_{p_2}}{\dot{m}_{ib}} \tag{41}$$

and a total recovery ratio for the system

$$\mathrm{RR} = \frac{\dot{m}_{p_1} + \dot{m}_{p_2}}{\dot{m}_f} = \mathrm{RR}_1 + \mathrm{RR}_2(1 - \mathrm{RR}_1) \tag{42}$$

The salinity of the brine at each stage is determined via a solute balance on each exchanger and by assuming a pure permeate stream. While RO membranes have a high solute rejection of $\geq$99%, assuming the permeate salinity is zero is an idealization [61]. In practice, large concentration gradients across the membrane will be present during brine concentration and salt flux will cause the permeate salinity to be greater than zero during operation.[7]

$$w_{s,ib} = \frac{w_{s,f}}{1 - \mathrm{RR}_1} \tag{43}$$

$$w_{s,b} = \frac{w_{s,ib}}{1 - \mathrm{RR}_2} \tag{44}$$

The specific work can now be expressed as the total work required for the five pumps shown in Fig. 18:

$$\frac{\dot{W}}{\dot{m}_p} = \frac{1}{\eta_p}\left[\left(\frac{1}{\mathrm{RR}}\right)\frac{2\ \mathrm{bar} - P_0}{\rho_f} + \left(\frac{1}{\mathrm{RR}} - 1\right)\left(\frac{P_{H_1} - P_{\mathrm{rec}_1}}{\rho_f} + \frac{P_{H_2} - P_{\mathrm{rec}_2}}{\rho_{ib}}\right) + \frac{\Delta P_{H_1} - 2\ \mathrm{bar}}{\rho_f} + \left(1 - \frac{\mathrm{RR}_1}{\mathrm{RR}}\right)\frac{P_{H_2} - \Delta P_{\mathrm{loss}}}{\rho_{ib}}\right] \tag{45}$$

The independent variables for calculating the specific work are the salinities of the feed $w_{s,f}$ and brine $w_{s,b}$ stream, the intermediate brine salinity $w_{s,ib}$, and the intermediate pressure P_{im}, where $2\ \mathrm{bar} < P_{im} < P_b$. If both booster pumps have the same efficiency, and to ensure that $P_{\mathrm{rec}_1} \leq P_{H_1}$ and $P_{\mathrm{rec}_2} \leq P_{H_2}$, the intermediate pressure can be arbitrarily chosen to lie between:

$$P_b - \frac{P_{H_2} - P_{ib}}{\eta_{PX}}\frac{\rho_b}{\rho_{ib}} < P_{im} < \frac{P_{H_1} - 2\ \mathrm{bar}}{\eta_{PX}}\frac{\rho_b}{\rho_f} + 2\ \mathrm{bar} \tag{46}$$

The intermediate brine salinity $w_{s,ib}$ is chosen to minimize the total work, which satisfies

$$\frac{\partial\left(\dot{W}/\dot{m}_p\right)}{\partial w_{s,ib}} = \left(\frac{\partial \Pi}{\partial w}\right)_{w_{s,ib}}\left(\frac{w_{s,ib}^2\,\rho_{ib}}{\rho_f} - w_{s,f}w_{s,ib}\right) - w_{s,f}\left(\Pi_b - \Pi_{ib} - \Delta P_{\mathrm{loss}}\right) = 0 \tag{47}$$

where we assume, for simplicity, that ρ_{ib} is independent of salinity. (The equation including terms that involve the derivative of density w.r.t. salinity is given in Appendix E). If we make the further approximations that

[7] If we were to place an additional two-stage RO unit to treat the concentrated permeate and assume that the permeate concentration is bounded at 1%, then the additional work to completely purify the permeate should not exceed 4 kWh/m^3.

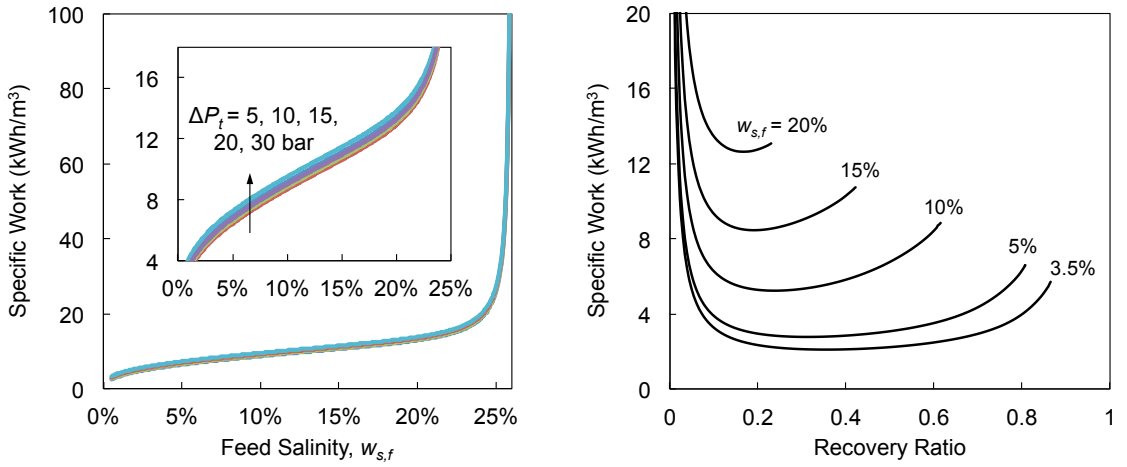

(a) $w_{s,b} = 26\%$ (b) $\Delta P_t = 10$ bar

Figure 19: Energetic figures of merit for RO: The specific work is shown to increase with increasing feed salinity, and rise in an unbounded manner as the more feed is pressurized for smaller permeate (RR $\to 0$). The inset in Fig. 19a shows the specific work vs. feed salinity for a narrower range of feed salinity to clearly display the effect of pinch.

$\Delta P_{\text{loss}} \ll (\Pi_b - \Pi_{ib})$ and introduce van 't Hoff's law for the osmotic pressure, Eq. (47) can be solved for the optimum value of intermediate brine salinity, $w^\star_{s,ib}$.

$$w^\star_{s,ib} = \sqrt{\frac{\rho_f}{\rho_{ib}} w_{s,f} w_{s,b}} \tag{48}$$

where we see that $w^\star_{s,ib}$ is proportional to the geometric mean of the feed and brine salinities.

The energy consumption is plotted against feed salinity for a fixed brine salinity and shown in Fig. 19a. The figure shows that the specific work rises until a feed salinity of about 23%, where it begins to rise rapidly as the feed salinity approaches saturation. Mathematically, this asymptote arises because the specific work is inversely proportional to RR [Eq.(45)], which approaches zero as the feed approaches the brine salinity. Physically, this behavior results from a large flow being pressurized and depressurized irreversibly for very little permeate as the recovery diminishes. Dividing the least work of separation by the specific work from Fig. 19a, we can plot the second law efficiency as shown in Fig. 20. A maximum efficiency of 62.7% occurs at a feed salinity of roughly 20% for $\Delta P_t = 15$ bar.

3.7. System Comparison

The models presented here allow for the comparison of different systems' energy efficiencies to better inform purchasing decisions and research directions. Choosing typical values for the pinches in each system (ΔT_t, ΔT_{pp}, and ΔP_t) allows the efficiency-salinity behavior of all the systems to be compared in a single plot, Fig. 21. Although the hypothetical two-stage RO system has the highest efficiency for a significant portion of the salinity domain, its proportional energetic advantage is not as significant at high salinity. Because these curves are sensitive to the choice of pinch, however, the exact tradeoffs will depend on the details of the system designs (e.g., ΔT_t in the MVC evaporator-condenser, the number of stages in the MED system, and to a lesser extent on the ΔP_t in the RO unit). Small scale systems in particular may be operated at higher pinches and have higher energy consumption.

The various systems respond differently to increased salinity. The efficiency of each system at typical seawater ($w_{s,f} = 3.5\%, w_{s,b} = 7\%$)[8] and produced water ($w_{s,f} = 15\%, w_{s,b} = 26\%$) salinities are shown in Fig. 22. Because the energy consumption of the evaporative systems at fixed brine salinity is less sensitive

[8] At seawater salinities, FO regeneration is more efficiently accomplished with RO (as described by Nicoll [62]), so we include FO-RO efficiency (see Appendix C) in Fig. 22.

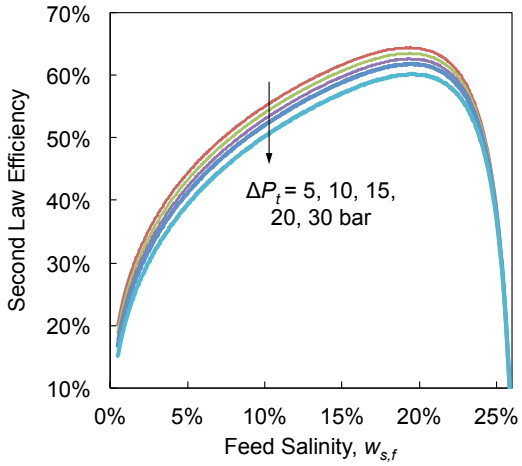

Figure 20: The second law efficiency increases with increasing feed salinity until about 23%, after which it drops as the recovery ratio diminishes and a large feed flow is irreversibly pressurized and depressurized to produce a small quantity of permeate.

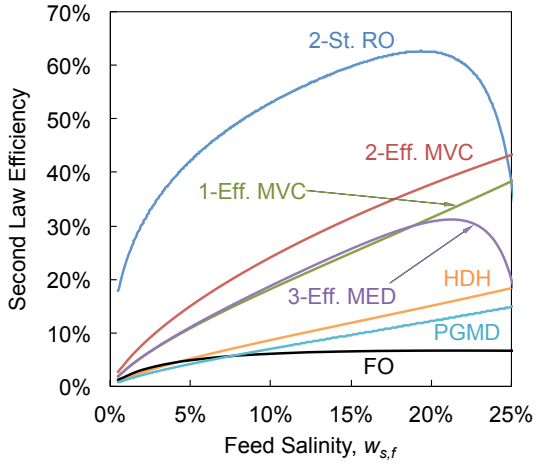

Figure 21: A comparison of system efficiencies over varying feed salinities shows that the hypothetical RO system generally outperforms exisiting produced water technologies.

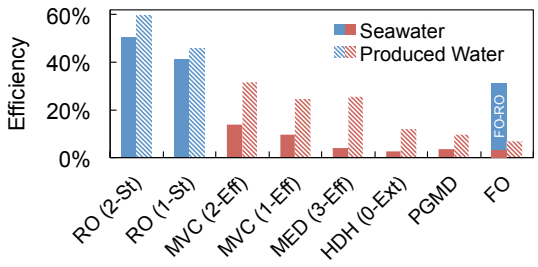

Figure 22: A comparison of efficiencies at seawater and typical produced water salinities shows that evaporative systems operate much closer to their limit at high salinities. Although energy is only a part of net system cost, the results show that RO has the potential to provide significant energy savings if realized for high salinities.

to feed salinity than RO, but the least work is a strong function of salinity (see Sec. 2), we see in Fig. 22 that the evaporative systems perform much closer to the reversible limit at the higher salinities encountered in produced water treatment. The efficiency of RO, on the contrary, does not change significantly between seawater and produced water salinities.

The difference between the RO and thermal systems' response to increased salinity is essentially driven by a combination of economics and design, where economics dictate the pinch (ΔT_t, ΔT_{pp}, and ΔP_t) and design dictates the level of imbalance[9]. For RO, the irreversible work is small compared to the reversible work across the entire salinity range. The result is high efficiency over the whole range. For MVC, the reversible work is small compared to the irreversible work at low salinities, but more comparable at high salinities, resulting in an efficiency increase at higher salinities. Essentially, the additional energy input required to achieve a finite pinch in an RO system is small relative to the osmotic pressure rise; in MED and MVC, the additional energy input required to achieve a practical temperature pinch is significant compared to the BPE rise at high salinities.

It is important to emphasize that lower energy consumption does not necessarily lead to lower cost. Some small scale systems that run primarily on thermal energy inputs may be able to take advantage of lower cost energy sources, despite higher energy consumption. Pretreatment costs must too be taken into account, and will be system-specific. High efficiency, of course, can also always be achieved at high cost with large system sizes, large heat exchangers, and large numbers of stages. Ultimately, because technology selection is always based on minimum cost, thermodynamics can inform but cannot dictate this choice.

4. Conclusions

The effects of increased salinity on desalination system performance have been investigated in the context of produced water. Based on produced water composition, we first conclude that:

- Whereas the rule of thumb for the least work required to desalinate seawater at 50% recovery is about 1 kWh/m^3, the minimum work required to desalinate produced water depends on the salinity but can be up to 9 kWh/m^3—nearly an order of magnitude higher.

Efficiency models were developed for MVC, MED, FO, HDH, PGMD, and a hypothetical RO system. Considering a fixed brine salinity of 26%, we can draw the following conclusions about the performance of each system:

- For single effect MVC, the energy consumption ranges from about 23–42 kWh/m^3, depending mainly on the system size and compressor efficiency. The primary effect of salinity on energy consumption is the increase in BPE within the evaporator condenser, requiring a higher discharge pressure in the compressor. A two-effect MVC system can require as little as 20 kWh/m^3 to treat produced water at medium-large scale.

[9]Imbalance is the uneven distribution of irreversibilties within a system, which would cause a system's efficiency to be less than 100% even with infinitely-sized exchangers [63].

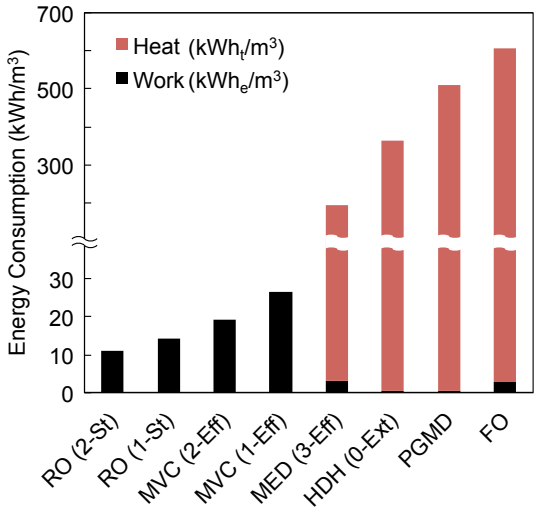

Figure 23: Thermal and electrical energy consumption of various desalination technologies under typical produced water conditions ($w_{s,f} = 15\%$, $w_{s,b} = 26\%$, medium-large scale).

- For MED, the GOR ranges from about 3–7, depending on the number of effects and the feed salinity. At higher feed salinities (lower recovery), MED behaves more like multistage flash, where large BPEs in the feed heaters penalize heat recovery and diminish GOR.
- For FO with thermal regeneration, an exergetic input of 25–150 kWh/m^3 is required, depending on the size of the FO unit and the efficiency of the draw regeneration process. Most of the exergy destruction occurs in the thermal draw regeneration step, so future efforts should focus on improving regeneration efficiency.
- For zero-extraction HDH, the GOR ranges from 1–3, depending on the system size and brine salinity. With brine recirculation, the GOR of HDH is generally independent of feed salinity. Alternate configurations with extraction and injection may improve performance.
- For PGMD, the GOR ranges from about 1–2, depending on system size and salinity. Like HDH, because it is inherently low recovery in a single pass, brine recirculation is required to obtain high RR. Alternate configurations, like multi-stage MD, can be used to effect better heat recovery and improve GOR.
- For a hypothetical two-stage RO system, energy inputs range from about 4–16 kWh/m^3, depending on the salinity and system size. Because the feed must be pressurized above the osmotic pressure of the brine, the system tends to perform best at moderate recovery ratios, where the imbalance in the RO unit is not too high and the amount of product per unit feed is not too low.

With regard to system performance in the produced water context, the following comparative conclusions have been drawn:

- Comparing a hypothetical two-stage RO system to systems currently compatible with high salinity shows that RO would still provide the best energy efficiency over a broad salinity range, except when operated at very low recovery. This efficiency advantage, however, is smaller at salinities well above the oceanographic range.
- Because the energy consumption of evaporative systems tends to be less sensitive to changes in salinity than RO under the selected pinches, but the least work of separation changes significantly with salinity, the efficiency of evaporative systems tends to be higher at higher feed salinities.

Acknowledgements

The authors would like to thank the King Fahd University of Petroleum and Minerals for funding the research reported in this paper through the Center for Clean Water and Clean Energy at MIT and KFUPM under project numbers R4-CW-08 and R13-CW-10. EWT and LDB acknowledge that this material is based upon work supported by the National Science Foundation Graduate Research Fellowship Program under Grant No. 1122374. HWC acknowledges funding by the Cooperative Agreement between the Masdar Institute of Science and Technology, Abu Dhabi, UAE and the Massachusetts Institute of Technology (MIT), Cambridge, MA, USA, Reference no. 02/MI/MI/CP/11/07633/GEN/G/00.

[1] "Produced water pretreatment for water recovery and salt production," Tech. Rep. 08122-36, Research Partnership to Secure Energy for America, 2012.

[2] U. S. Department of Energy and the National Energy Technology Laboratory, "Modern Shale Gas Development in the United States: A Primer," 2009.

[3] S. A. Holditch, "Getting the gas out of the ground," *Chemical Engineering Progress*, vol. 108, pp. 41–48, August 2012.

[4] C. E. Clark and J. A. Veil, "Produced Water Volumes and Management Practices in the United States," September 2009.

[5] U. S. Energy Information Agency, "Annual Energy Outlook 2013," 2013.

[6] T. Smith, "Environmental considerations of shale gas development," *Chemical Engineering Progress*, vol. 108, pp. 53–59, August 2012.

[7] M. Bomgardner, "Treating water from hydraulic fracturing," *Chemical & Engineering News*, vol. 90, pp. 13–16, October 2012.

[8] S. Rassenfoss, "From Flowback to Fracturing: Water Recycling Grows in the Marcellus Shale," *Journal of Petroleum Technology*, vol. 63, no. 7, pp. 48–51, 2011.

[9] K. M. Keranen, M. Weingarten, G. A. Abers, B. A. Bekins, and S. Ge, "Sharp increase in central Oklahoma seismicity since 2008 induced by massive wastewater injection," *Science*, 2014.

[10] W. L. Ellsworth, "Injection-induced earthquakes," *Science*, vol. 341, pp. 142–149, July 2013.

[11] K. M. Keranen, H. M. Savage, G. A. Abers, and E. S. Cochran, "Potentially induced earthquakes in Oklahoma, USA: Links between wastewater injection and the 2011 M_w 5.7 earthquake sequence," *Geology*, vol. 41, no. 6, pp. 699–702, 2013.

[12] S. Horton, "Disposal of hydrofracking waste fluid by injection into subsurface aquifers triggers earthquake swarm in central Arkansas with potential for damaging earthquake," *Seismological Research Letters*, vol. 83, pp. 250–260, March/April 2012.

[13] Ohio Department of Natural Resources, "Preliminary Report on the Northstar 1 Class II Injection Well and the Seismic Events in the Youngstown, Ohio Area," tech. rep., 2012.

[14] D. L. Shaffer, L. H. A. Chavez, M. Ben-Sasson, S. R.-V. Castrilln, N. Y. Yip, and M. Elimelech, "Desalination and reuse of high-salinity shale gas produced water: Drivers, technologies, and future directions," *Environmental Science and Technology*, vol. 47, pp. 9569–9583, 2013.

[15] T. Hayes and B. F. Severin, "Barnett and Appalachian shale water management and reuse technologies," Tech. Rep. 08122-05, Research Partnership to Secure Energy for America, 2012.

[16] R. Wasylishen, "Recycling flowback and produced water in tight-oil development," *Desalination & Water Reuse*, vol. 22, no. 2, pp. 26–30, 2013.

[17] T. Pankratz, ed., "HDH tackles brine dispoal challenge," *Water Desalination Report*, vol. 50, no. 17, pp. 2–3, 2014.

[18] R. K. McGovern, S. M. Zubair, and J. H. Lienhard V, "The cost effectiveness of electrodialysis for diverse salinity applications," *Desalination*, vol. 348, pp. 57–65, 2014.

[19] G. P. Thiel, S. M. Zubair, and J. H. Lienhard V, "An analysis of likely scalants in the treatment of produced water from Nova Scotia," *Heat Transfer Engineering*, vol. 36, pp. 652–662, 2015.

[20] G. P. Thiel and J. H. Lienhard V, "Treating produced water from hydraulic fracturing: composition effects on scale formation and desalination system selection," *Desalination*, vol. 346, pp. 54–69, 2014.

[21] K. S. Pitzer, "Thermodynamics of Electrolytes. I. Theoretical Basis and General Equations," *Journal of Physical Chemistry*, vol. 77, no. 2, pp. 268–277, 1973.

[22] K. S. Pitzer and J. J. Kim, "Thermodynamics of Electrolytes. IV. Activity and Osmotic Coefficients for Mixed Electrolytes," *Journal of the American Chemical Society*, vol. 96, pp. 5701–5707, September 1974.

[23] J. F. Zemaitis, D. M. Clark, M. Rafal, and N. C. Scrivner, *Handbook of Aqueous Electrolyte Thermodynamics*. Wiley-AIChE, 1986.

[24] K. S. Pitzer, "A thermodynamic model for aqueous solutions of liquid-like density," *Reviews in Mineralogy and Geochemistry*, vol. 17, pp. 97–142, 1987.

[25] W. Wagner and H.-J. Kretzschmar, *International Steam Tables*. Springer, 2nd ed., 2008.

[26] K. H. Mistry, M. A. Antar, and J. H. Lienhard V, "An improved model for multiple effect distillation," *Desalination and Water Treatment*, vol. 51, pp. 807–821, 2013.

[27] K. H. Mistry, H. A. Hunter, and J. H. Lienhard V, "Effect of composition and nonideal solution behavior on desalination calculations for mixed electrolyte solutions with comparison to seawater," *Desalination*, vol. 318, pp. 34–47, 2013.

[28] K. H. Mistry and J. H. Lienhard V, "General least energy of separation for desalination and other chemical separation processes," *Entropy*, vol. 15, pp. 2046–2080, May 2013.

[29] K. H. Mistry and J. H. Lienhard V, "Effect of nonideal solution behavior on desalination of a sodium chloride (NaCl) solution and comparison to seawater," *Journal of Energy Resources Technology*, vol. 135, June 2013.

[30] K. H. Mistry, R. K. McGovern, G. P. Thiel, E. K. Summers, S. M. Zubair, and J. H. Lienhard V, "Entropy generation analysis of desalination technologies," *Entropy*, vol. 13, no. 10, pp. 1829–1864, 2011.

[31] A. Saul and W. Wagner, "International equations for the saturation properties of ordinary water substance," *Journal of Physical and Chemical Reference Data*, vol. 16, no. 4, pp. 893–901, 1987.

[32] H. T. El-Dessouky and H. M. Ettouney, *Fundamentals of Salt Water Desalination*. Elsevier, 2002.

[33] G. M. Zak and A. Mitsos, "Hybrid thermal-thermal desalination structures," *Desalination and Water Treatment*, vol. 52, no. 16–18, pp. 2905–2919, 2014.

[34] Y. M. El-Sayed and R. S. Silver, *Principles of Desalination*, ch. Fundamentals of Distillation, pp. 55–109. New York, NY: Academic Press, 2nd ed., 1980.

[35] B. D. Coday, P. Xu, E. G. Beaudry, J. Herron, K. Lampi, N. T. Hancock, and T. Y. Cath, "The sweet spot of forward osmosis: Treatment of produced water, drilling wastewater, and other complex and difficult liquid streams," *Desalination*, vol. 333, no. 1, pp. 23–35, 2014.

[36] R. L. McGinnis, N. T. Hancock, M. S. Nowosielski-Slepowron, and G. D. McGurgan, "Pilot demonstration of the NH3/CO2 forward osmosis desalination process on high salinity brines," *Desalination*, vol. 312, pp. 67–74, 2013.

[37] S. Lee, C. Boo, M. Elimelech, and S. Hong, "Comparison of fouling behavior in forward osmosis (FO) and reverse osmosis (RO)," *Journal of Membrane Science*, vol. 365, no. 1-2, pp. 34–39, 2010.

[38] R. Semiat, J. Sapoznik, and D. Hasson, "Energy aspects in osmotic processes," *Desalination and Water Treatment*, vol. 15, no. 1-3, pp. 228–235, 2010.

[39] R. L. McGinnis and M. Elimelech, "Energy requirements of ammonia-carbon dioxide forward osmosis desalination," *Desalination*, vol. 207, no. 13, pp. 370–382, 2007.

[40] V. Darde, W. J. M. van Well, E. H. Stenby, and K. Thomsen, "Modeling of carbon dioxide absorption by aqueous ammonia solutions using the extended UNIQUAC model," *Industrial & Engineering Chemistry Research*, vol. 49, no. 24, pp. 12663–12674, 2010.

[41] D. D. Wagman, *The NBS tables of chemical thermodynamic properties: Selected values for inorganic and C1 and C2 organic substances in SI units*. American Chemical Society and the American Institute of Physics for the National Bureau of Standards., 1982.

[42] E. W. Tow, R. K. McGovern, and J. H. Lienhard V, "Raising forward osmosis brine concentration efficiency through flow rate optimization," *Desalination*, in press, 2015, doi: http://dx.doi.org/10.1016/j.desal.2014.10.034.

[43] Y. Demirel, "Thermodynamic analysis of separation systems," *Separation Science and Technology*, vol. 39, no. 16, pp. 3897–3942, 2004.

[44] S. Zhang, P. Wang, X. Fu, and T.-S. Chung, "Sustainable water recovery from oily wastewater via forward osmosis-membrane distillation (FO-MD)," *Water Research*, vol. 52, pp. 112–121, 2014.

[45] A. Altaee and G. Zaragoza, "A conceptual design of low fouling and high recovery FO-MSF desalination plant," *Desalination*, vol. 343, pp. 2–7, 2013.

[46] E. W. Tow and J. H. Lienhard V, "Experiments and modeling of bubble column dehumidifier performance," *International Journal of Thermal Sciences*, vol. 80, pp. 65–75, 2014.

[47] G. P. Narayan, M. H. Sharqawy, S. Lam, S. K. Das, and J. H. Lienhard V, "Bubble columns for condensation at high concentrations of non-condensable gas: Heat transfer model and experiments," *AIChE Journal*, vol. 59, no. 5, pp. 1780–1790, 2013.

[48] E. W. Tow and J. H. Lienhard V, "Heat transfer to a horizontal cylinder in a shallow bubble column," *International Journal of Heat and Mass Transfer*, vol. 79, pp. 353–361, 2014.

[49] K. M. Chehayeb, G. P. Narayan, S. M. Zubair, and J. H. Lienhard V, "Use of multiple extractions and injections to thermodynamically balance the humidification dehumidification desalination system," *International Journal of Heat and Mass Transfer*, vol. 68, pp. 422–434, 2014.

[50] G. P. Thiel, J. A. Miller, and J. H. Lienhard V, "Effect of mass extractions and injections on the performance of a fixed-size humidification-dehumidification desalination system," *Desalination*, vol. 314, pp. 50–58, 2013.

[51] R. K. McGovern, G. P. Thiel, G. P. Narayan, S. M. Zubair, and J. H. Lienhard V, "Performance limits of zero and single extraction humidification-dehumidification desalination systems," *Applied Energy*, vol. 102, pp. 1081–1090, 2013.

[52] G. P. Narayan, K. Chehayeb, R. K. McGovern, G. P. Thiel, S. M. Zubair, and J. H. Lienhard V, "Thermodynamic balancing of the humidification dehumidification desalination system by mass extraction and injection," *International Journal of Heat and Mass Transfer*, vol. 57, pp. 756–770, 2013.

[53] G. P. Thiel and J. H. Lienhard V, "Entropy generation in condensation in the presence of high concentrations of noncondensable gases," *International Journal of Heat and Mass Transfer*, vol. 55, pp. 5133–5147, September 2012.

[54] W. Wagner and A. Pruß, "The IAPWS formulation 1995 for the thermodynamic properties of ordinary water substance for general and scientific use," *Journal of Physical and Chemical Reference Data*, vol. 31, no. 2, pp. 387–535, 2002.

[55] D. Singh and K. K. Sirkar, "Desalination of brine and produced water by direct contact membrane distillation at high temperatures and pressures," *Journal of Membrane Science*, vol. 389, pp. 380–388, 2012.

[56] L. Francis, N. Ghaffour, A. Alsaadi, and G. Amy, "Material gap membrane distillation: a new design for water vapor flux enhancement," *Journal of Membrane Science*, vol. 448, pp. 240–247, 2013.

[57] E. K. Summers, H. A. Arafat, and J. H. Lienhard V, "Energy efficiency comparison of single stage membrane distillation (MD) desalination cycles in different configurations," *Desalination*, vol. 290, pp. 54–66, 2012.

[58] L. D. Nghiem, T. Ren, N. Aziz, I. Porter, and G. Regmi, "Treatment of coal seam gas produced water for beneficial use in australia: A review of best practices," *Desalination and Water Treatment*, vol. 32, pp. 316–323, 2011.

[59] A. Zhu, P. D. Christofides, and Y. Cohen, "Effect of thermodynamic restriction on energy cost optimization of RO membrane water desalination," *Industrial & Engineering Chemistry Research*, vol. 48, pp. 6010–6021, 2009.

[60] A. Zhu, A. Rahardianto, P. Christofides, and Y. Cohen, "Reverse osmosis desalination with high permeability membranes - cost optimization and research needs," *Desalination and Water Treatment*, vol. 15, pp. 256–266, 2010.

[61] M. Wilf, *The Guidebook to Membrane Desalination Technology*. Balaban Desalination Publications, 2007.

[62] P. Nicoll, "Forward osmosis as a pre-treatment to reverse osmosis," in *Proceedings of the International Desalination Association World Congress on Desalination and Water Reuse, Tianjin, China, Oct 20-25*, 2013. Paper #TIAN13-121.

[63] G. P. Thiel, R. K. McGovern, S. M. Zubair, and J. H. Lienhard V, "Thermodynamic equipartition for increased second law efficiency," *Applied Energy*, vol. 118, pp. 292–299, 2014.

[64] K. S. Pitzer, J. C. Peiper, and R. H. Busey, "Thermodynamic properties of aqueous sodium chloride solutions," *Journal of Physical and Chemical Reference Data*, vol. 13, pp. 1–102, 1984.

[65] R. C. Phutela, K. S. Pitzer, and P. P. S. Saluja, "Thermodynamics of aqueous magnesium chloride, calcium chloride, and strontium chloride at elevated temperatures," *Journal of Chemical and Engineering Data*, vol. 32, pp. 76–80, 1987.

[66] D. J. Bradley and K. S. Pitzer, "Thermodynamics of Electrolytes. 12. Dielectric Properties of Water and Debye-Hückel Parameters to 350° C and 1 kbar," *The Journal of Physical Chemistry*, vol. 83, no. 12, pp. 1599–1603, 1979.

[67] R. K. McGovern, J. P. Mizerak, S. M. Zubair, and J. H. Lienhard V, "Three dimensionless parameters influencing the optimal membrane orientation for forward osmosis," *Journal of Membrane Science*, vol. 458, pp. 104–110, 2014.

[68] DOW FILMTEC Membranes, "SW30HR-380 High Rejection Seawater RO Element Product Manual," 2013.

[69] DOW FILMTEC Membranes, "SW30XHR-440i Seawater Reverse Osmosis Element Product Manual," 2013.

[70] TORAY Membranes, "TM800M Standard SWRO Product Manual," July 2013.

[71] Nitto Denko - Hydranautics, "Hydranautics membrane brochure," 2002.

[72] J. M. Gozalvez, J. Lora, J. A. Mendoza, and M. Sancho, "Modelling of a low-pressure reverse osmosis system with concentrate recirculation to obtain high recovery levels," *Desalination*, vol. 144, no. 13, pp. 341–345, 2002.

[73] C. W. Wohlert, "Apparatus and methods for solution processing using reverse osmosis," 2012.

[74] M. T. M. Pendergast, J. M. Nygaard, A. K. Ghosh, and E. M. Hoek, "Using nanocomposite materials technology to understand and control reverse osmosis membrane compaction," *Desalination*, vol. 261, no. 3, pp. 255–263, 2010. Special Issue in memory of Sidney Loeb (1917-2008).

[75] Lenntech bv - CodeLine, "CodeLine Pressure Vessels 40E100-6 Specifications Sheet," 2014.

Appendix A. Thermophysical Properties

Appendix A.1. Pitzer Equations

The Pitzer model for thermophysical properties has been widely applied to mixed electrolytes at high ionic strengths. It is based on a virial expansion of the Gibbs free energy, and accounts for ion interactions through pairwise and ternary parameters. Derivations can be found in, e.g., [21, 22, 24]. The excess Gibbs free energy is given by

$$\begin{aligned}\frac{G^{\mathrm{ex}}}{m_w RT} = F &+ \sum_c \sum_a b_c b_a [2B_{ca} + ZC_{ca}] \\ &+ \sum_{c<c'} \sum b_c b_{c'} \left[2\Phi_{cc'} + \sum_a b_a \Psi_{cc'a} \right] \\ &+ \sum_{a<a'} \sum b_a b_{a'} \left[2\Phi_{aa'} + \sum_c b_c \Psi_{caa'} \right] \end{aligned} \tag{A.1}$$

where

$$F = -\frac{4A^\phi I}{1.2} \ln(1 + 1.2\sqrt{I}) \tag{A.2}$$

$$A^\phi = \frac{1}{3} \left[\frac{e^3 \left(2N_0 \rho_w\right)^{1/2}}{8\pi \left(\epsilon_r \epsilon_0 k_b T\right)^{3/2}} \right] \tag{A.3}$$

$$B_{ij} = \beta_{ij}^{(0)} + \beta_{ij}^{(1)} g(\alpha\sqrt{I}) \tag{A.4}$$

$$g(x) = \frac{2}{x^2}[1 - (1 + x)\exp(-x)] \tag{A.5}$$

$$Z = \sum_i b_i |z_i| \tag{A.6}$$

$$\Phi_{ij} = \theta_{ij} + {}^E\theta_{ij}(I) \tag{A.7}$$

and $\alpha = 2.0\ \mathrm{kg}^{\frac{1}{2}}/\mathrm{mol}^{\frac{1}{2}}$, N_0 is Avogadro's number, e is the elementary charge, ϵ_r is the relative permittivity of pure water, ϵ_0 is the vacuum permittivity, and k_b is the Boltzmann constant. The parameters $\beta_{ij}^{(0)}$, $\beta_{ij}^{(1)}$, C_{ij}, θ_{ij}, and Ψ_{ijk} represent specific ion interactions and are tabulated. The term ${}^E\theta_{ij}(I)$ accounts for certain electrostatic in asymmetric electrolytes and must be computed by numerical integration as described in [24]. Values and correlations for the Pitzer parameters are from [64] for NaCl; for $CaCl_2$ they are taken from [65]. Equations for the dielectric constant as a function of temperature and pressure are given by Bradley and Pitzer [66], and data for the thermophysical properties of water are taken from IAPWS [25]. Contributions to the excess Gibbs free energy from uncharged solutes can be represented by additional terms in Eq. (A.1) as required.

With the Pitzer parameters in terms of temperature and pressure, G^{ex} can be appropriately differentiated to obtain the thermophysical properties of interest: the excess heat capacity, excess volume, and the osmotic coefficient. The excess volume is

$$V^{\mathrm{ex}} = \left(\frac{\partial G^{\mathrm{ex}}}{\partial P} \right)_T \tag{A.8}$$

$$= \frac{A^V I}{1.2} \ln(1 + 1.2\sqrt{I}) + RT \left\{ \sum_c \sum_a b_c b_a \left[2B_{ca}^V + ZC_{ca}^V \right] + \ldots \right\} \tag{A.9}$$

where

$$A^V = 2A^\phi RT\left[3\left(\frac{\partial \ln \epsilon_r}{\partial P}\right)_T - \beta_w\right] \tag{A.10}$$

$$B^V = \left(\frac{\partial B}{\partial P}\right)_T \tag{A.11}$$

$$C^V = \left(\frac{\partial C}{\partial P}\right)_T \tag{A.12}$$

and β_w is the isothermal compressibility of water.

The excess molal specific heat capacity is

$$c_p = -\frac{T}{m_w M_w}\left(\frac{\partial^2(G^\circ + G^{\text{ex}})}{\partial T^2}\right)_P \tag{A.13}$$

$$= \frac{\bar{c}^\circ_{p,w}}{M_w} + \sum_i b_i \bar{c}^\circ_{p,i} + c_p^{\text{ex}} \tag{A.14}$$

$$\frac{c_p^{\text{ex}}}{RT^2} = \frac{A^J I}{RT^2 1.2}\ln(1+1.2\sqrt{I}) - \sum_c\sum_a b_c b_a\left[2B^J_{ca} + ZC^J_{ca}\right] + ... \tag{A.15}$$

where

$$A^J = 4RT^2\left[\left(\frac{\partial A^\phi}{\partial T}\right)_P + \frac{2}{T}\left(\frac{\partial^2 A^\phi}{\partial T^2}\right)_P\right] \tag{A.16}$$

$$B^J = \left(\frac{\partial B}{\partial T}\right)_P + \frac{2}{T}\left(\frac{\partial^2 B}{\partial T^2}\right)_P \tag{A.17}$$

$$C^J = \left(\frac{\partial C}{\partial T}\right)_P + \frac{2}{T}\left(\frac{\partial^2 C}{\partial T^2}\right)_P \tag{A.18}$$

The osmotic coefficient is

$$\phi - 1 = \frac{-1}{RT\sum_i b_i}\left(\frac{\partial G^{\text{ex}}}{\partial m_w}\right) \tag{A.19}$$

$$= \frac{2}{\sum_i b_i}\left[\frac{-A^\phi I^{3/2}}{1+1.2\sqrt{I}} + \sum_c\sum_a b_c b_a (B^\phi_{ca} + ZC_{ca}) + ...\right] \tag{A.20}$$

where

$$B^\phi_{ij} = \beta^{(0)}_{ij} + \beta^{(1)}_{ij}\exp\left(-\alpha\sqrt{I}\right) \tag{A.21}$$

Appendix A.2. Effective Boiling Point Elevation

The effective boiling point elevation, δ_{eff}, is the difference in temperature when the enthalpy difference between a saturated moist air mixture above a pure and saline solution is zero. That is, δ_{eff} satisfies

$$(h_g + \omega^s h_v)\Big|_{T,P,m=0} = (h_g + \omega^s h_v)\Big|_{T+\delta_{\text{eff}},P,m} \tag{A.22}$$

Values of δ_{eff} are provided in Table A.1.

Appendix B. Least Work Curve

The least work of separation as a function of feed salinity for various brine salinities is shown in Fig. B.1 below.

Table A.1: The effective boiling point elevation (in K) for aqueous NaCl

	b_{NaCl} (mol/kg)					
T (°C)	1	2	3	4	5	6
25	0.4318	0.9081	1.447	2.059	2.750	3.523
30	0.4774	1.0060	1.605	2.284	3.048	3.900
35	0.5204	1.0990	1.754	2.495	3.328	4.253
40	0.5612	1.1860	1.894	2.695	3.591	4.583
45	0.5996	1.2690	2.027	2.882	3.837	4.892
50	0.6362	1.3470	2.153	3.060	4.070	5.181
55	0.6712	1.4230	2.273	3.229	4.290	5.454
60	0.7051	1.4950	2.388	3.390	4.500	5.713
65	0.7376	1.5640	2.499	3.546	4.702	5.961
70	0.7694	1.6320	2.606	3.695	4.895	6.197
75	0.8002	1.6970	2.710	3.839	5.081	6.424
80	0.8303	1.7610	2.810	3.979	5.260	6.642

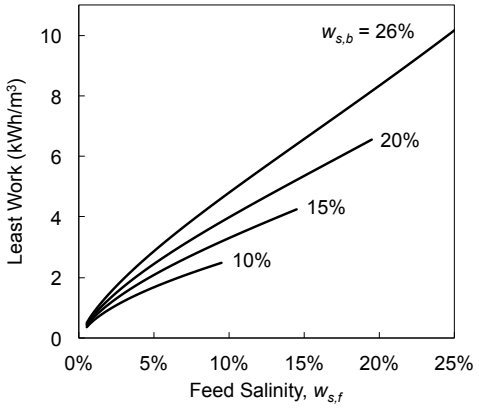

Figure B.1: The least work can be up to an order of magnitude higher in produced water brine concentration applications than for seawater at 50% recovery.

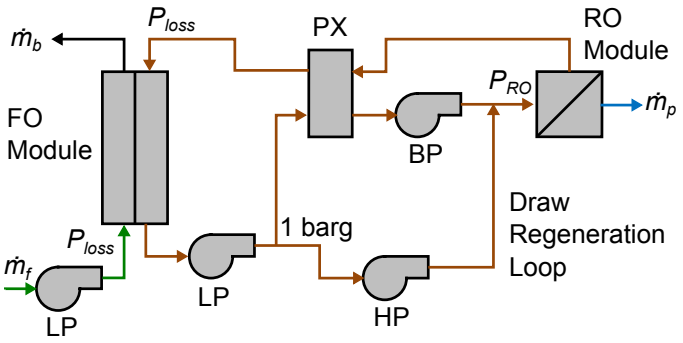

Figure C.1: Schematic diagram of FO-RO for seawater desalination

Appendix C. Seawater FO-RO Model

The energy consumption of seawater FO-RO shown in Fig. 22 is calculated using the model described here. For the FO-RO system depicted in Fig. C.1, we find that the energy consumption of FO-RO is:

$$\frac{\dot{W}}{\dot{m}_p} = \frac{1}{\eta_p}\left(\frac{\rho_p}{\rho_{dd}}\frac{\mathrm{MR}}{\mathrm{RR}}\left[P_{RO} - (P_{RO} - 2\,\Delta P_{\mathrm{loss}})\eta_{PX}\frac{\rho_{dd}}{\rho_{dc}}\right] + \frac{\rho_p}{\rho_{dd}}P_{RO} + \frac{\rho_p}{\rho_f}\frac{1}{\mathrm{RR}}\Delta P_{\mathrm{loss}}\right), \tag{C.1}$$

where the RO operating pressure is $P_{RO} = \Pi_b + \Delta\Pi_{t,FO} + \Delta\Pi_{t,RO} + 2\,\Delta P_{\mathrm{loss}}$ and the mass ratio is

$$\mathrm{MR} = \mathrm{RR}\frac{w_{s,dd}}{w_{s,dc} - w_{s,dd}}, \tag{C.2}$$

and the dilute and concentrated draw salinities are $w_{s,dd} = \Pi_f + \Delta\Pi_{t,FO} - \Delta P_{\mathrm{loss}}$ and $w_{s,dc} = \Pi_b + \Delta\Pi_{t,FO} + \Delta P_{\mathrm{loss}}$, respectively, as determined by balancing the FO exchanger to have a fixed terminal hydraulic-osmotic pressure pinch [42]. ΔP_{loss} is the hydraulic pressure loss through the FO channels. Exchanger hydraulic pressure drop, pump efficiency and pressure exchanger efficiency were consistent with the RO model, Sec. 3.6. FO pressure pinch is assumed to be larger (20 bar) than that of the RO unit due to more significant internal concentration polarization [67]. Using this model, the power consumption of seawater FO-RO at 50% recovery is estimated to be 3.60 kWh/m^3, which is slightly greater than that of seawater RO but much less than that of seawater FO with thermal regeneration.

Appendix D. Challenges with RO in the Produced Water Sector

There are two major obstacles to using RO in the produced water sector. The first is the very high pressures required to use RO membranes to concentrate what can be an already highly saline stream. During RO operation, the applied pressure must be greater than the osmotic pressure of the brine. For seawater RO, for a 35 g/kg feed at 50% recovery, the brine stream reaches roughly 70 g/kg which corresponds to a brine osmotic pressure, and a minimum applied hydraulic pressure, of 60.1 bar for an NaCl solution. At the solubility limit of NaCl, the maximum extent to which concentration is possible, the osmotic pressure reaches an extraordinarily high value of 379.2 bar. Instead of concentrating to the solubility limit, however, one may find it economical to concentrate the brine stream to within 20 to 30 g/kg of the limit and then route the brine to a crystallizer to finish the process.

Another obstacle is the high cost of the extensive pre-treatment required. Thermal systems are more robust and the effect of stream composition on cleaning intensity and frequency is less severe than for membrane based systems.

There are several major concerns with operating RO at high pressures. The first is the ability of the membrane and support structure to withstand the applied pressures. Currently, seawater RO membranes across three manufacturers are only rated to withstand a maximum operating pressure of 69–83 bar [68–71]. Sources in literature have investigated the effect of increasing the osmotic pressure on the permeate side in order to reduce the top pressure required for desalination. One way to increase the osmotic pressure on the permeate side is to recirculate the brine stream to the permeate side at a lower hydraulic pressure [72].

Another way is to tier multiple RO systems. This would be done by repeatedly splitting feed and product streams in two, pressurizing one stream, and allowing both streams to flow through a counterflow exchanger [73].

Also, at high pressures, the permeability of TFC membranes can drastically decrease due to structural compaction. Pendergast et al. [74] found that, at modest pressures of 34 bar, the decrease in permeability can range from 21–70% and the increase in solute rejection can range from 76–98%. A similar deterioration in permeability and improvement in salt rejection can be expected for higher pressures. A deterioration in permeability will require more membrane area to achieve the same recovery ratio as a membrane which does not undergo structural compaction.

The third obstacle to high pressure RO is the increased chance of scaling and fouling. The combination of high recovery and extremely diverse compositions encountered in produced waters treatment can lead to a wide variety of scaling and fouling problems [20]. This is especially prevalent in RO at very near bulk saturation, when concentration polarization causes supersaturation near the membrane surface.

Lastly, the structural integrity of the pressure vessels must be maintained at high pressures. Seawater RO pressure vessels are rated to 69 bar of operating pressure but have a burst pressure of 414 bar [75]. Raising the top pressure a pressure vessel can withstand simply requires increasing the thickness of the vessel. The added materials will increase the plant's capital expenditure.

Appendix E. Optimum Intermediate Brine Salinity in Two-Stage Hypothetical RO

The optimum intermediate brine salinity for minimizing the specific energy of the two-stage reverse osmosis process shown in Fig. 18 is determined by taking a first order derivative of Eq. (45) w.r.t. $w_{s,ib}$. Including the terms which involve the derivative of density we find:

$$\begin{aligned}\frac{\partial\left(\dot{W}/\dot{m}_p\right)}{\partial w_{s,ib}} = &\left(\frac{\partial \Pi}{\partial w_s}\right)_{w_{s,ib}} \left(\frac{w_{s,ib}^2\,\rho_{ib}}{\rho_f} - w_{s,f} w_{s,ib}\right) - w_{s,f}\left(\Pi_b - \Pi_{ib} - \Delta P_{\text{loss}}\right) \\ &- \left(\frac{\partial \rho}{\partial w_s}\right)_{w_{s,ib}} \frac{1}{\rho_{ib}^2}\left[\left(1 - \frac{\text{RR}_1}{\text{RR}}\right)\left(\Delta P_{\text{loss}} + \Pi_b - \Pi_{ib}\right)\right. \\ &\left. + \left(\frac{1}{\text{RR} - 1}\right)\left(\Delta P_{\text{loss}} + \Pi_b - \Pi_{ib} - 2\text{ bar} - \eta_{\text{PX}}\frac{\rho_{\text{f}}}{\rho_{\text{b}}}\left(\rho_{im} - 2\text{ bar}\right)\right)\right] = 0 \end{aligned} \tag{E.1}$$